Three-dimensional director structures of defects in Grandjean-Cano wedges of cholesteric liquid crystals studied by fluorescence confocal polarizing microscopy

I. I. Smalyukh and O. D. Lavrentovich*

Chemical Physics Interdisciplinary Program and Liquid Crystal Institute, Kent State University, Kent, Ohio 44242

We use a nondestructive technique of fluorescence confocal polarizing microscopy to visualize three-dimensional director patterns of defects in Grandjean-Cano wedges filled with a cholesteric liquid crystal of pitch $p = 5$ μm. Strong surface anchoring of the director causes a stable lattice of dislocations in the bulk. Optical slicing in the vertical cross sections of the wedges allows us to establish the detailed structure of dislocations and their kinks. Dislocations of Burgers vector $b = p/2$ are located in the thin part of the sample, very close to the bisector plane. Their cores are split into a pair of $\tau^{-1/2}$ and $\lambda^{+1/2}$ disclinations. Pairs of $\lambda^{-1/2}$ and $\tau^{+1/2}$ disclinations are observed when the $b = p/2$ dislocation forms a kink. The kinks along the $b = p/2$ dislocations change the level of dislocations by $\pm p/4$ and $\pm p/2$; these kinks are confined to the glide plane and are very long, $(5-10)$ p. Above some critical thickness h_c of the wedge sample, the dislocations are of Burgers vector $b = p$. They are often found away from the bisector plane. The core of $b = p$ dislocations is split into a pair of nonsingular $\lambda^{-1/2}$ and $\lambda^{+1/2}$ disclinations. The kinks along the $b = p$ dislocation are of a typical size p and form cusps in the direction perpendicular to the glide plane. At the cusp, $\lambda^{-1/2}$ and $\lambda^{+1/2}$ disclinations interchange ends. Other defect structures inlude "Lehmann clusters," i.e., dislocations of zero Burgers vector formed by two $\lambda^{-1/2}$ and two $\lambda^{+1/2}$ disclinations and dislocations of nonzero Burgers vector with a core split into more than two disclinations. We employ the coarse-grained Lubensky–de Gennes model of the cholesteric phase to describe some of the observed features. We calculate the elastic energy of a dislocation away from the core, estimate the energy of the core split into disclinations of different types, study the effect of finite sample thickness on the dislocations energy, and calculate the Peach-Koehler elastic forces that occur when a dislocation is shifted from its equilibrium position. Balance of the dilation/compression energy in the wedge and the energy of dislocations defines the value of h_c and allows to estimate the core energy of the dislocations. Finally, we consider the Peierls-Nabarro mechanisms hindering glide of dislocations across the cholesteric layers. Because of the split disclination character of the core, glide is difficult as compared to climb, especially for $b = p$ dislocations.

I. INTRODUCTION

Cholesteric liquid crystals (CLCs) have a twisted ground state with helical configuration of the director **n**, which specifies the average local orientation of molecules. External fields and surface interactions can easily deform the ideal helicoidal configuration. When the spatial scale of distortions is much larger than the cholesteric pitch p (corresponding to the director twist by 2π), elastic properties of CLCs are similar to those of smectic phases with a one-dimensional periodic structure [1,2]. If a CLC is confined within a finite volume, the equilibrium structure is determined by bulk elasticity and boundary effects, such as surface tension and surface anchoring. Very often, the boundary conditions are satisfied by the appearance of large-scale defects such as focal conic domains, curvature walls, dislocations, etc. [3–6].

Confinement-induced distortions in cholesterics are usually studied in the so-called Grandjean-Cano wedges. A CLC fills a dihedron with a small angle, formed, for example, by a pair of mica or glass plates. As first observed by Grandjean [7], a lattice of defect lines forms parallel to the edge. The lines separate different Grandjean zones, the regions of cell with a different number N of the director rotations by π. The defect lattice is apparently stabilized by (a) stresses caused by dihedron geometry and (b) strong surface anchoring at the plates. Subsequent polarizing-microscopy observations and analysis [8–16] have established three types of lines in the Grandjean lattice. The line closest to the edge is a "Moebius disclination" with a planar director twist, separating a nontwisted region from a region twisted by π [15]. It is followed by "thin lines" that are edge dislocations with Burgers vectors $b = p/2$. Farther away, for thicknesses larger than some critical value h_c, one finds "thick lines" representing edge dislocations with $b = p$. Thin and thick dislocations are split into pairs of disclinations. Geometry dictates two different ways of splitting [13]: a thin line $b = p/2$ splits into τ and λ disclinations and a thick line $b = p$ splits into a $\lambda\lambda$ or $\tau\tau$ pair of disclinations. The nomenclature here, introduced by Kleman and Friedel [13], is based on the notation λ for the local director **n**, χ for the direction of the helical axis, and $\tau = \lambda \times \chi$. In λ disclinations, the material λ director field is nonsingular, while in τ disclinations, λ is singular and τ is not. Both types of lines are parallel to the cholesteric layers, except near the kinks, which change the level of the edge dislocations along the helicoid axis [15]. Generally, at least for the small-molecular-weight LCs, the pair representing $b = p/2$ dislocation is $\tau^{-1/2}\lambda^{+1/2}$, and $b = p$ is represented by

*Corresponding author. Email address: odl@lci.kent.edu

$\lambda^{-1/2}\lambda^{+1/2}$ pair [15,16]; the first symbol refers to the disclination closer to the thin end of the sample. However, there are also reports that the pairs might be of $\lambda^{-1/2}\tau^{+1/2}$ and even $\tau^{-1/2}\tau^{+1/2}$ type, see, e.g., Ref. [17]. The superscripts in notations such as $\tau^{-1/2}$ and $\lambda^{+1/2}$ correspond to the director winding number around the disclination. In terms of the Volterra process "$-$" sign corresponds to adding material between the lips separated by an angle π, and "$+$" sign corresponds to material removal [3,5,6].

Although there have been a great deal of studies on confined cholesteric samples, there are still problems to explore, such as the detailed core structure of split dislocations, the relationship between h_c and the energy of elastic distortions around dislocations, the structure and elastic properties of kinks along the dislocations, the role of the boundary conditions in the stability and the location of dislocation lines within the bounded sample, etc. Recent findings [18] indicate that when the confining plates set in-plane degenerate alignment, then the defect lines are not observed at all. Studies for smectic samples with free surfaces, see, for example, the review paper by Holyst and Oswald [19], demonstrate that surface tension at the smectic-air interface can dramatically influence the equilibrium location of the dislocation. The value of the critical sample thickness h_c has been related [12] to the distance L between two thick lines as $h_c = kL$. The numerical constant has been originally reported as $k = 2 \pm 0.3$ [12]; however, this constant might be in fact smaller, $k = 0.12 \pm 0.03$, according to Durand [20]; see also recent estimates by Pieranski and Oswald [21]. A model by Nallet and Prost [22] establishes how the Burgers vector of dislocations changes with the local thickness h in smectic A (Sm-A) wedges. Although the cholesteric case is formally similar to the smectic case as long as the coarse-grained model [1,2] is valid, the properties of the Grandjean-Cano lattices in CLC and Sm-A wedges should be different, as (1) the core structure of elementary dislocations is different (core size of the order of lamellar spacing, or one molecular length, ~ 1 nm in thermotropic smectics and 1–10 μm in CLC, depending on the pitch); (2) surface anchoring energies are different (tilted orientation of Sm-A layers is associated with the anchoring energy $\sim (10^{-2} - 10^{-3})$ J/m^2 [23] much larger than the corresponding values $\sim (10^{-4} - 10^{-6})$ J/m^2 for CLCs with p in the range (0.5–15) μm [24–26]).

An adequate experimental technique to study the problems listed above seems to be fluorescence confocal polarizing microscopy (FCPM) [27,28]. The advantage of FCPM technique over the regular polarizing microscopy (PM) is that it allows to reconstruct a three-dimensional (3D) director structure by visualizing thin (~ 1 μm) optical slices of the sample in both horizontal and vertical planes. The technique is nondestructive, unlike the electron microscopy [29,17] of polymerized or otherwise modified samples. Although the sample in FCPM studies is stained with a fluorescent dye, the concentration of dopant is extremely small, about 0.01%.

In this paper we employ the FCPM technique to explore the structural properties of dislocation patterns in Grandjean-Cano cholesteric wedges. We present optical slices of the textures and establish the 3D director patterns corresponding to local (core structure) and global (location within the sample, layers distortions) features of dislocations and associated kinks. Experiments are performed for well-equilibrated samples and for transient textures. Using a coarse-grained model [1,2] of CLCs, we analyze the stability of thick and thin lines and their interaction with the substrates. We calculate the far-field energy of layer distortion around an edge dislocation, and confinement-induced corrections to this energy (in approximation of infinitely strong anchoring). These results allow one to determine the relative stability of dislocations with $b = p/2$ and $b = p$, their line energy, explain the difference in the shape of kinks (which are long when formed along the $b = p/2$ dislocations and short along the $b = p$ dislocations), analyze the Peierls-Nabarro friction energies, and to find the critical thickness h_c. The calculations are in good agreement with the experimental data.

II. EXPERIMENTAL TECHNIQUES

A. Materials and cell preparation

To form a CLC, we mixed a nematic LC material ZLI2806 with a chiral dopant CB15 (both purchased from EM Industries). The nematic matrix has the following properties: dielectric anisotropy $\Delta\varepsilon = -4.8$, Frank elastic constants $K_1 = 14.9$ pN (splay), $K_2 = 7.9$ pN (twist), $K_{33} = 15.4$ pN (bend), clearing point $T_{NI} = 101$ °C, and birefringence $\Delta n \approx 0.045$. For the FCPM observations, the cholesteric mixture is doped with a very small amount (0.01 wt %) of fluorescent dye n,n'-bis(2,5-di-tert-butylphenyl)-3,4,9,10-perylenedicarboximide (BTBP), purchased from Molecular Probes [27,28].

CLC samples of maximum thickness 100 μm were confined between pairs of glass plates with transparent indium tin oxide (ITO) electrodes to enable application of the electric field. The thickness h of cells was measured by interference method. The dihedron angle α of wedge cells was measured using reflected laser beam for empty cells (in all experiments $\alpha < 2$ °). To minimize spherical aberrations in FCPM observations with an immersion oil objectives, we used glass substrates of thickness 0.15 mm with refractive index 1.52.

Planar alignment was set by a unidirectionally rubbed (along the thickness gradient, Fig. 1) polyimide PI-2555 (HD MicroSystems) film spin coated over the ITO layers. The director is in the plane of the substrate with a possible small pretilt angle $\lesssim 1$ °. The polar anchoring coefficient W_p, characterizing the work needed to deviate **n** from the easy axis in the vertical plane, is expected to be of the order of 10^{-4} J/m^2, as this is a typical value measured for PI2555 in contact to a variety of nematic mixtures with a positive dielectric anisotropy, see Ref. [30]; azimuthal anchoring coefficient is smaller, $W_a \sim 10^{-5}$ J/m^2 [31].

B. Fluorescence confocal polarizing microscopy

The FCPM technique links the director orientation to the intensity of measured fluorescent signal [27,28]. Compared to the well-known fluorescence confocal microscopy (FCM), FCPM has two distinctive features: (a) the specimen is

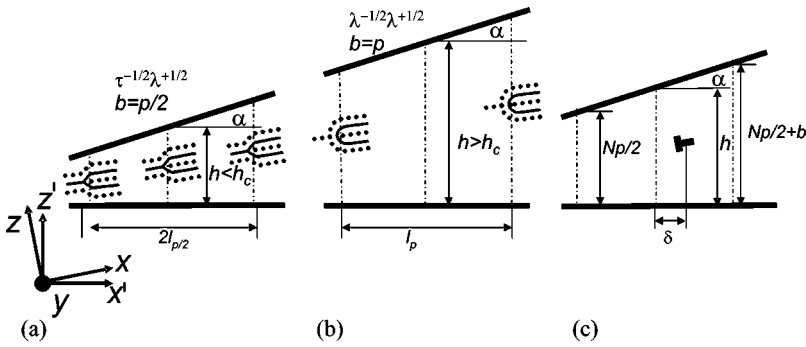FIG. 1. Grandjean-Cano cholestetric wedge with a lattice of (a) dislocations $b = p/2$ stable at $h < h_c$ and (b) dislocations $b = p$ at $h > h_c$; (c) introduces notations used in text and shows climb of a dislocation toward its equilibrium position in the bisector plane.

stained with *anisometric* dye molecules (in this case, BTBP) that follow the director orientation; (b) the excitation light is *polarized*, usually linearly.

The FCPM setup was assembled on the basis of Olympus Fluoview BX-50 reflective-mode confocal microscope, Fig. 2. The excitation beam (488 nm, Ar laser) is focused by an objective into a small (< 1 μm^3) volume within the CLC slab. The fluorescent light from this volume is detected by a photomultiplier tube in the spectral region 510–550 nm. A pinhole discriminates against the regions above and below the selected volume [32]. The pinhole size D is adjusted according to magnification and numerical aperture (NA) of the objective; $D = 100$ μm for an immersion oil $60\times$ objective with NA$= 1.4$. The polarizer $\mathbf{P}$ determines polarization of both the excitation beam $\mathbf{P}_e$, and the detected fluorescent light $\mathbf{P}_f$: $\mathbf{P}_f \| \mathbf{P}_e \| \mathbf{P}$. The beam power is small, ≈ 120 nW, to avoid light-induced reorientation of the dye-doped LC [33].

For BTBP dye, the fluorescence lifetime $\tau_F = (3.7 – 3.9)$ ns [34] is smaller than the characteristic time of rotational diffusion $\tau_D \sim 10$ ns, and dye orientations during absorption and emission can be assumed to be close to each other [28]. The FCPM signal, resulting from a sequence of absorption and emission, strongly depends on the angle β between the transition dipole (parallel to the local director $\mathbf{n}$ in our system) and $\mathbf{P}$: $I \sim \cos^4 \beta$ [27,28], as both absorption and emission follow the dependency $\cos^2 \beta$. The strongest FCPM signal corresponds to $\mathbf{n} \| \mathbf{P}$ ($\beta = 0$), and sharply de-

creases when β becomes nonzero.

The focused beam scans the sample at a fixed depth $-h/2 \leq z \leq h/2$, creating a "horizontal" optical slice $I(x,y)$. The scanning is repeated at different depths, to obtain a stack of optical slices, i.e., a 3D pattern $I(x,y,z)$, related to the 3D pattern $\mathbf{n}(x,y,z)$ through the dependence $I \sim \cos^4 \beta$. Note that the correspondence $I(x,y,z) \leftrightarrow \mathbf{n}(x,y,z)$ is not unique when only one fixed direction of linear polarization $\mathbf{P}$ is used, as the angular parameter β defines a cone of directions. To avoid ambiguity, we use different directions of the linear polarization $\mathbf{P}$ [e.g., $\mathbf{P} = (P,0,0)$ and $\mathbf{P} = (0,P,0)$] and also a circularly polarized light. In the latter case, only the changes
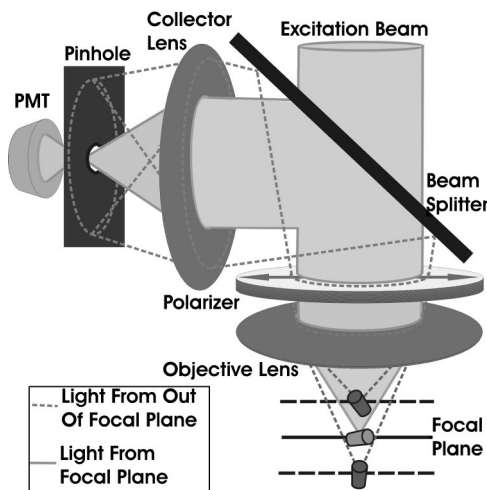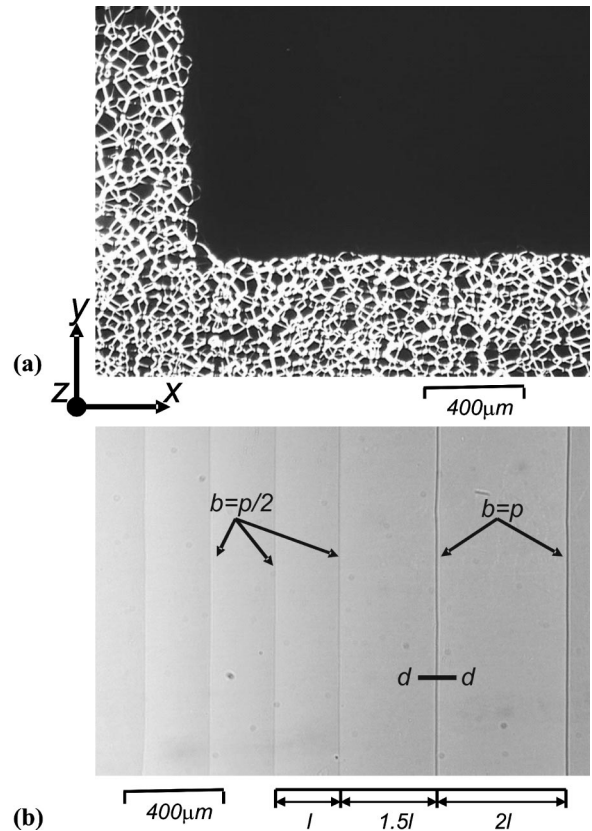

(a)

(b)

FIG. 3. Polarizing microscopy textures of unstable and stable defects in cholesteric cells: (a) a flat sample, $h = 10$ μm; $p = 1$ μm; defects in the area coated by the electrodes are removed by an ac field (50 V); (b) a wedge sample, $p = 5$ μm, $\alpha = 0.45°$; stable lattice of $b = p/2$ and $b = p$ dislocations. A vertical cross section along the line dd is shown in Fig. 4(d).
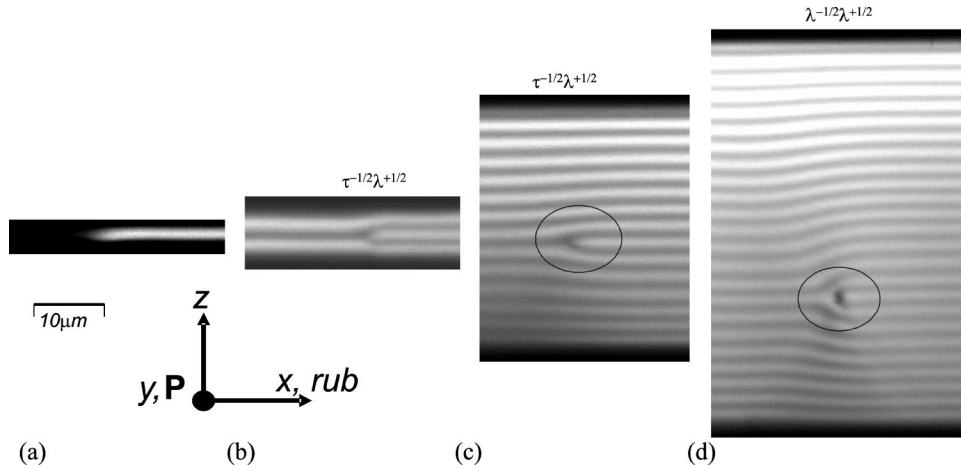

FIG. 2. Setup for the fluorescence confocal polarizing microscopy.

FIG. 4. FCPM textures of vertical x-z cross sections of Grandjean-Cano wedge with right-handed CLC, $p = 5$ μm, strong planar anchoring: (a) twist disclination separating 0π and 1π Grandjean zones; (b) $b = p/2$ dislocation with a core split into a $\tau^{-1/2}\lambda^{+1/2}$ disclination pair, separating 2π and 3π Grandjean zones; (c) the same, between 13π and 14π zones; (d) $b = p$ dislocation with a core split into a $\lambda^{-1/2}\lambda^{+1/2}$ disclination pair, 22π and 24π zones, the slice obtained along the bb line in Fig. 3(b). Polarizer **P** is parallel to the y axis. The rubbing direction is along the x axis. Bright regions correspond to $\mathbf{n}\|\mathbf{P}$, darker regions correspond to $\mathbf{n}\perp\mathbf{P}$ or bounding glass plates.

in the vertical component n_z of the director are detected; n_x and n_y are not discriminated against each other. Using computer software, the 3D pattern $I(x,y,z)$ can be cut by vertical planes such as $(x$-$z)$ and $(y$-$z)$ to visualize **n** across the sample.

Low birefringence $\Delta n \approx 0.045$ of the nematic host mitigates two problems that one encounters in FCPM imaging of CLCs: (1) relative defocusing of extraordinary versus ordinary modes [27] and (2) the Mauguin effect (polarization of light follows the twisted director) [28]. To maintain both axial and radial resolution within 1 μm, we used relatively shallow ($\leqslant 60$ μm) depth of scanning [28]. Furthermore, with $p \approx 5$ μm, the Mauguin parameter $\Delta n p/2\lambda \approx 0.2$ is small, so that light propagates in the so-called short-wavelength circular regime with almost circularly polarized eigenmodes [35]; their interference produces a wave with a polarization state close to that of the excitation beam, so that the relationship $I \sim \cos^4\beta$ remains valid [28]. Finally, note that in the FCPM images of thick (>30 μm) samples, the registered fluorescence signal from the bottom of the cell is somewhat weaker than from the top, as a result of finite light absorption, depolarization, and defocusing.

III. EXPERIMENTAL RESULTS

Usually, in a flat cell, defects such as oily streaks and dislocations are metastable objects caused by the material flow during the cell filling. These defects eventually relax to the equilibrium planar state $\boldsymbol{\chi}\|\mathbf{z}$; the relaxation is slow (can take months). To reduce the relaxation time, we used a cholesteric LC with $\Delta\varepsilon < 0$ so that the applied electric field $\mathbf{E}\|\mathbf{z}$ facilitates the equilibrium planar state $\boldsymbol{\chi}\|\mathbf{z}$, Fig. 3(a). In the Grandjean-Cano wedge with strong surface anchoring, the defects correspond to the equilibrium state and persist even when an external field is applied, Fig. 3(b). The dislocation lines are aligned along the y axis, their Burgers vectors are along the z axis, thus the glide plane is the y-z plane. Note that in order to present the experimental and theoretical results in the most compact form, we use two Cartesian coordinate frames, rotated with respect to each other by the angle $\alpha/2$ around the y axis: (x,y,z) and (x',y,z'), where the x axis is along the bisector of the wedge and the x' axis is along the bottom plate; $x' = x = 0$ at the edge.

A. Equilibrated samples

The whole 3D director structure can be understood by combining the regular PM textures, Fig. 3(b), and the FCPM cross sections in the vertical plane x-z that contains the thickness gradient direction, Fig. 4. The thin part of the wedge contains thin dislocations parallel to the y axis and separated by distances $l \approx p/(2\tan\alpha)$, as measured in the (x',y,z') frame. For $h > h_c$, one observes a lattice of thick
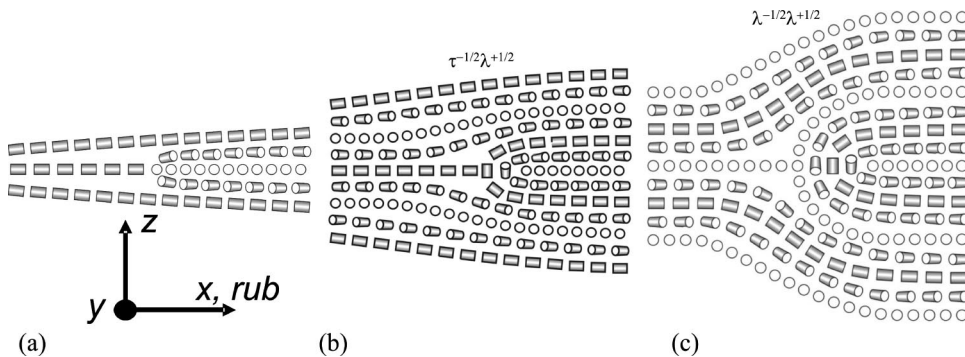

FIG. 5. Director configurations corresponding to (a) twist disclinations in Fig. 4(a); (b) $\tau^{-1/2}\lambda^{+1/2}$ disclination pair in Figs. 4(b,c); (c) $\lambda^{-1/2}\lambda^{+1/2}$ disclination pair in Fig. 4(d).

lines with a period $2l$. The distance between the last thin and the first thick line is $1.5l$, Fig. 3(b). The corresponding vertical cross sections reveal the basic features of the defects listed below.

(1) The first line separating 0π and 1π Grandjean zones is a twist disclination, Figs. 4(a) and 5(a), typical of a nematic, as the director experiences a slight splay remaining in the (x-z) plane to the left of the core and twists by π around the z axis in the region to the right of the core.

(2) The thin lines separating Grandjean zones in the thin part of the sample, $h<h_c$, [such as zones 2π and 3π, Fig. 4(b); 13π and 14π, Fig. 4(c)] are all separated by dislocations with the Burgers vector $\mathbf{b}=(0,0,1)p/2$. Their core is split into disclination pairs $\tau^{-1/2}\lambda^{+1/2}$, Fig. 5(b). Another possible splitting, into $\lambda^{-1/2}\tau^{+1/2}$ pairs, is observed in transient structures when the dislocation $b=p/2$ forms a kink, i.e., a step that brings the dislocation to a different z level, see point (1) in the following subsection. Predominance of $\tau^{-1/2}\lambda^{+1/2}$ pairs over $\lambda^{-1/2}\tau^{+1/2}$ pairs has been explained by Kleman [3]: the singular core in $\tau^{+1/2}$ line is less spread and thus costs more energy as compared to $\tau^{-1/2}$ singular core.

(3) The thick lines at $h>h_c$ are dislocations of Burgers vector $\mathbf{b}=b(0,0,1)$; $b=p$, Fig. 4(d), with the core split into a $\lambda^{-1/2}\lambda^{+1/2}$ pair with a continuous $\mathbf{n}$. Their singular counterparts, $\tau^{-1/2}\tau^{+1/2}$ pairs, are never observed, as the singular core would carry an additional elastic energy $\sim K\ln(p/r_c)$, where K is an average Frank constant and $r_c\ll p$ is the core size of the order of few molecular sizes [5].

(4) The critical thickness h_c of the wedge at which the lattice of $b=p/2$ dislocations is replaced with $b=p$ dislocations depends on the wedge dihedral angle α. Experimentally, for the studied range $5\ \mathrm{mrad}<\alpha<20\ \mathrm{mrad}$, $k=\alpha h_c/p\approx0.08$, Fig. 6, close to the Durand's data $k\approx0.12$ [20].
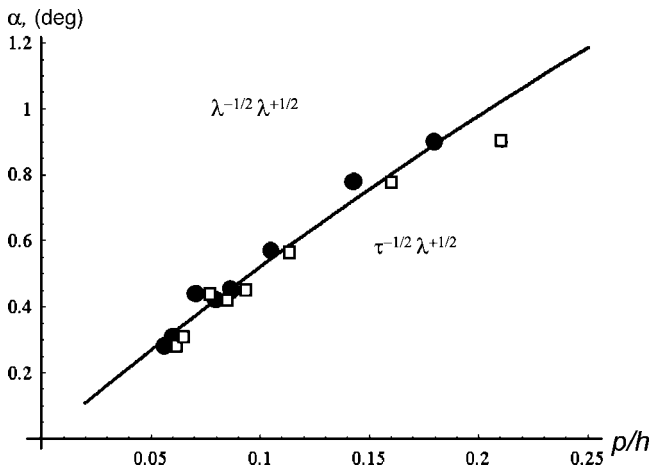

FIG. 6. Stability diagram of $\tau^{-1/2}\lambda^{+1/2}$ and $\lambda^{-1/2}\lambda^{+1/2}$ pairs as determined by locations of dislocations in wedge samples of different angle α. The squares denote the last $\tau^{-1/2}\lambda^{+1/2}$ pair met as one moves towards the thick part of the wedge; the circles mark the first $\lambda^{-1/2}\lambda^{+1/2}$ pair. The solid line shows the theoretical dependence $\alpha(p/h_c)$ obtained by comparing the energies Eqs. (31), (32) of the two dislocation structures, with the following parameters: $C_1=0.4$, $C_2=1$, $r_c=6$ nm, $K_2=7.9$ pN, $K_{33}=15.4$ pN.

B. Metastable structures: Kinks

Below we describe the defect textures that are not part of the equilibrium defect lattice and appear only as metastable features.

(1) *Kinks along $b=p/2$ dislocations*. In the studied wedges with a strong surface anchoring, both thin and thick lines are located in the bulk of the cell and never at the surfaces. Moreover, the $b=p/2$ dislocations accumulate in the bisector plane or not farther than $p/2$ from it. Initial filling of the cell might form $b=p/2$ dislocations in other locations, but they relatively quickly move to the middle plane. The lines do not glide as the whole, but via kinks, Figs. 7 and 8. There are two types of kinks: kinks of height $\pm p/4$, Fig. 7, and kinks of height $\pm p/2$, Fig. 8. The $\pm p/4$ kinks are more frequent; they are involved in the most common scenario of dislocation glide, in which one $\pm p/4$ kink moves along the dislocation line (along the y axis) thus changing its z coordinate by $p/4$ and transforming $\tau^{-1/2}\lambda^{+1/2}$ into $\lambda^{-1/2}\tau^{+1/2}$, and then a second kink propagates in the same direction to restore the pair $\tau^{-1/2}\lambda^{+1/2}$ that is now shifted by $p/2$ with respect to the original $\tau^{-1/2}\lambda^{+1/2}$. The core structure of $\pm p/4$ kink is intermediate between that of pure $\tau^{-1/2}\lambda^{+1/2}$ and $\lambda^{-1/2}\tau^{+1/2}$ states, Fig. 7. The $\pm p/2$ kinks can be seen near the nodes where $b=p/2$ dislocations join other line defects located at a different z level in the sample, e.g., $b=0$ dislocations, as described in more detail below in point (4). Such a $\pm p/2$ kink can be stable for hours, as the glide of defects with $b\neq p/2$ is very difficult. Figure 8(b) reveals the core structure of a $p/2$ kink in the glide plane; the core structure changes from $\tau^{-1/2}\lambda^{+1/2}$ into $\lambda^{-1/2}\tau^{+1/2}$ and then back to $\tau^{-1/2}\lambda^{+1/2}$ state along the y axis, Figs. 8(c,d,e).

There are two distinct features of both $\pm p/4$ and $\pm p/2$ kinks along the $b=p/2$ dislocations as compared to the kinks along $b=p$ dislocations [see point (2) below]. First, the $b=p/2$ kinks make a very small angle with the y axis; their characteristic length w is thus large, about $(5-10)p$, Figs. 7 and 8. Second, the kinks are confined to the glide plane of the parent $b=p/2$ dislocation, Fig. 8(b).

(2) *Kinks along $b=p$ dislocations*. The glide of $\lambda^{-1/2}\lambda^{+1/2}$ pairs with $b=p$, Fig. 4(d), is much more difficult as compared to $b=p/2$ dislocations; these pairs can remain in the locations away from the bisector plane for months. The kinks along $b=p$ dislocations were observed only in the specially prepared samples with *weak* surface anchoring (unrubbed polyisoprene coating) and with an applied electric field. When a voltage pulse of amplitude $V\gg V_c$ and duration ~ 1 sec is applied, a $b=p$ kink is generated (at the wedge of cell or at a spacer) and propagates along the edge dislocation, shifting its position by a distance p towards the middle plane. The $b=p$ kinks are relatively short and depart from the glide plane of the parent dislocation, Figs. 9–12.

Figure 9 presents a series of vertical FCPM slices taken in the vicinity of the kink, in the plane x-z normal to the dislocation. The planes of the vertical cross sections $1x$-z–$5x$-z are marked by straight lines on the optical slice $4y$-z (marked also $ABCD$), which contains the core of a $\lambda^{-1/2}$ disclination. The polarizer is along the y axis. Far from the kink (planes $1x$-z and $5x$-z), the core is a well-defined
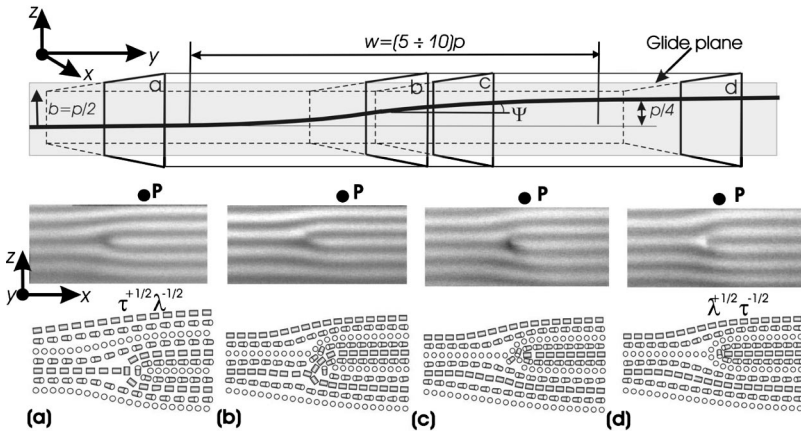
FIG. 7. FCPM textures of a kink of height $p/4$ along the dislocation $b=p/2$; the core $\tau^{-1/2}\lambda^{+1/2}$ (a) transforms into the $\lambda^{-1/2}\tau^{+1/2}$ core (d).

$\lambda^{-1/2}\lambda^{+1/2}$ pair. The vertical cross sections $2-4y\text{-}z$ in the vicinity of kink show a complex 3D structure in which the director at the core region is titled rather than normal to the planes $2x\text{-}z-4x\text{-}z$.
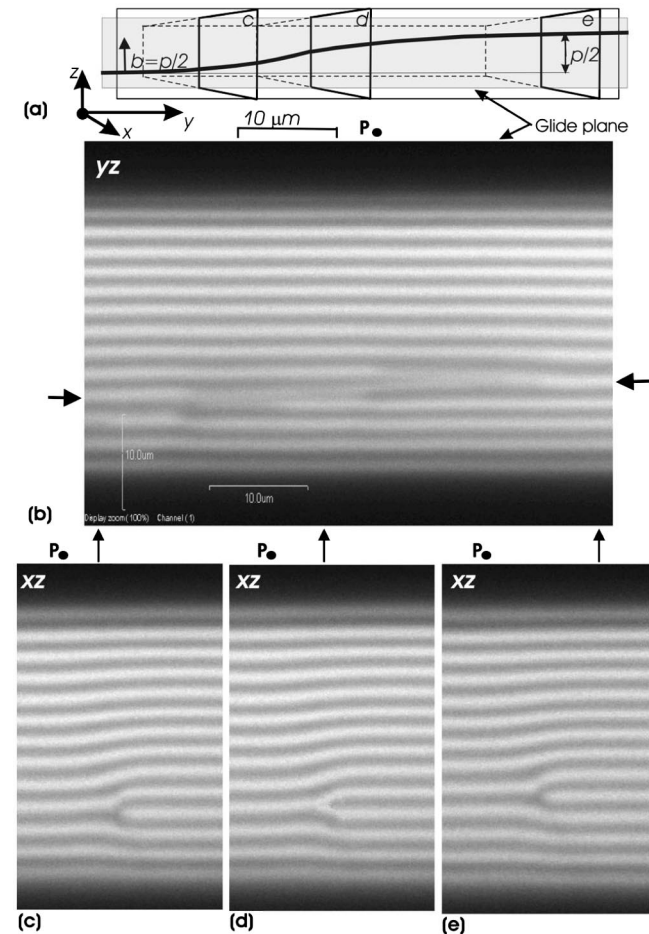

FIG. 8. FCPM textures of a kink of height $p/2$ along the dislocation $b=p/2$; (b) vertical cross section along the glide plane; the kink is only slightly tilted with respect to the parent dislocation, the horizontal arrows indicate the z levels where the kink ends; (c)–(e) vertical cross sections perpendicular to the glide plane that show how the core $\tau^{-1/2}\lambda^{+1/2}$ (c) transforms first into the $\lambda^{-1/2}\tau^{+1/2}$ core (d) and then back into the $\tau^{-1/2}\lambda^{+1/2}$ core (e).

In Fig. 10, the vertical optical slices $1y\text{-}z-9y\text{-}z$ are parallel to the glide plane. The orthogonal cross sections $10x\text{-}z$ and $11x\text{-}z$ are normal to the dislocation and demonstrate than the kink shifts the dislocation by p along the z axis. The plane $2y\text{-}z$ contains the $\lambda^{+1/2}$ disclination of the splitted core. The slices $2y\text{-}z-8y\text{-}z$ show that near the kink, the dislocation deviates from the y direction toward the thinner part of the wedge, Fig. 10, thus forming a cusp first noticed by Bouligand [15]. Using the principles described in Sec. II B, we reconstruct the 3D director field near the kink, Figs. 11 and 12, to visualize the details hidden for ordinary microscopy (the $\lambda^{+1/2}$ and $\lambda^{-1/2}$ lines are aligned on top of each other at the center of the cusp rather than side by side, as they normally are).

At the kink, both λ disclinations deviate from the y axis by $\pi/2$ and align along the x axis, each forming a cusp. The director in the core of each λ disclination remains parallel to the disclination axis, and thus the $\pi/2$ rotation of the disclination also means a shift of the core by $p/4$ along the z axis. The tilt preserves the nonsingularity of director field; without
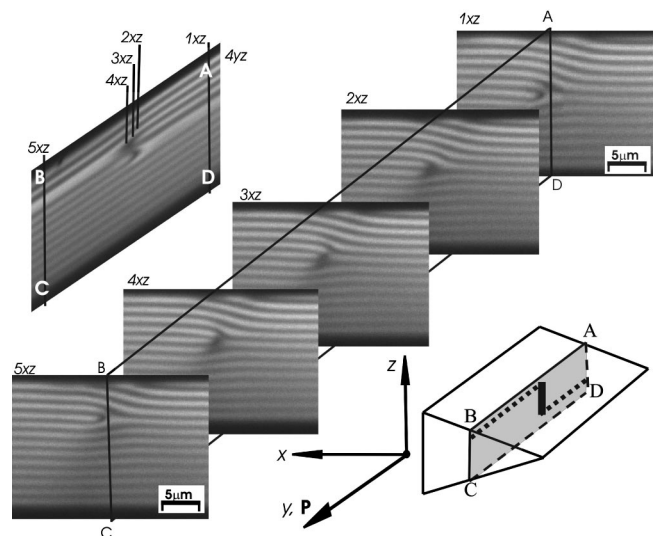

FIG. 9. FCPM textures of a kink of height $p/2$ along the dislocation $b=p$ as seen in the vertical planes $1x\text{-}z-5x\text{-}z$ normal to the dislocation; the plane $ABCD$ $4y\text{-}z$ contains the core of $\lambda^{-1/2}$ disclination.
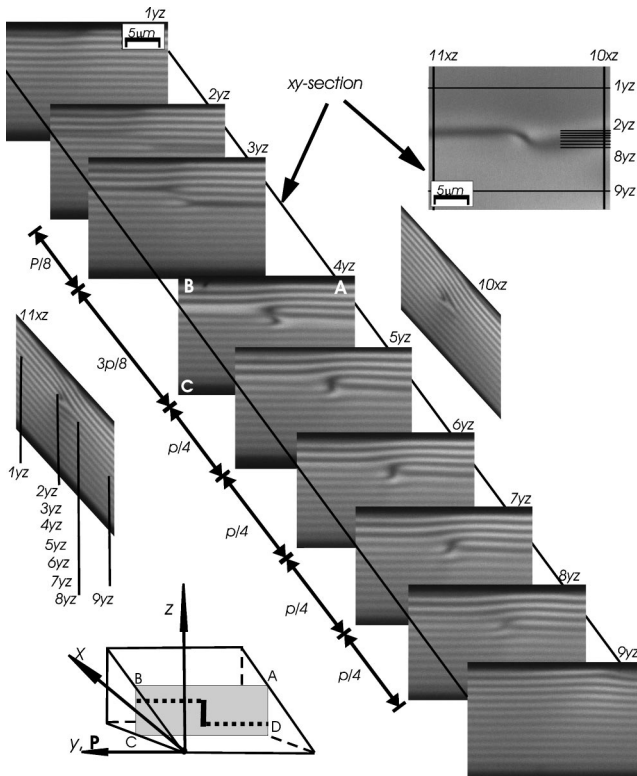
FIG. 10. FCPM textures of the same kink as in Fig. 9, as seen in the vertical planes $1y$-z–$9y$-z parallel to the plane ABCD $4y$-z. In the right top corner, a horizontal slice x-y demonstrates a cusp associated with the kink.

tilt, $\lambda^{-1/2}\lambda^{+1/2}$ would transform into a singular $\tau^{-1/2}\tau^{+1/2}$ core. At the cusp, the $\lambda^{-1/2}$ disclination entering the kink from one side transforms into a $\lambda^{+1/2}$ disclination leaving the kink on the other side, Fig. 12. The kink at $b=p$ dislocation, therefore, has a complex structure with a cusp and interchange of the $\lambda^{+1/2}$ and $\lambda^{-1/2}$ disclinations; its size is of the order of p along all three coordinate axes, Fig. 12.

(3) *Thick lines with* $b=p/2$. The thinner part of the wedge might contain transient structures of the total Burgers vector $b=p/2$ that appear as "thick" lines in standard PM observations. These configurations are in fact very different from the equilibrium pairs $\lambda^{-1/2}\lambda^{+1/2}$ observed in the thick part of the sample, as their core is composed of more than two disclinations. For example, Figs. 13(a) and 13(b) shows two close dislocations with the Burgers vectors $b_1=-p/2$ (pair $\tau^{+1/2}\lambda^{-1/2}$) and $b_2=p$ (pair $\lambda^{-1/2}\lambda^{+1/2}$), respectively. This structure quickly (within a few hours) relaxes into the equilibrium single dislocation $b=p/2$ (pair $\tau^{-1/2}\lambda^{+1/2}$) shown in Figs. 4(c), 5(b), and 13(e). Another example, Figs. 13(c) and 13(f), is also a combination of the same four disclinations (one $\lambda^{+1/2}$, two $\lambda^{-1/2}$'s, and one $\tau^{+1/2}$), topologically equivalent to a dislocation $b=p/2$. The structure relaxes to an equilibrium pair $\tau^{-1/2}\lambda^{+1/2}$ preserving the value $b=p/2$, Figs. 13(d) and 13(e) (the relaxation was accelerated by a 1 sec ac voltage pulse of 15 V). Restructuring usually starts at spacers or at the edge of cell and propagates along the defect bundle.
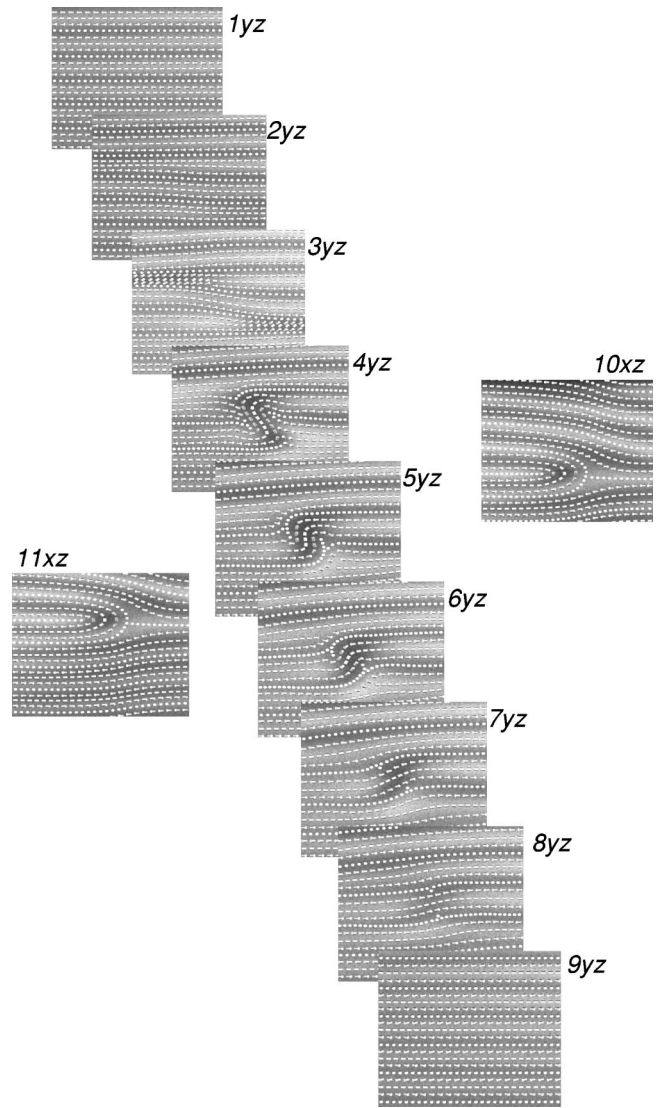

FIG. 11. Reconstructed director field of a kink along the dislocation $b=p$ shown in Figs. 9 and 10, as seen in y-z cross sections.

(4) *Defects of zero Burgers vector* $b=0$. One often finds thick lines that are *perpendicular* to the equilibrium dislocations and parallel to the thickness gradient of the wedge, Fig. 14. FCPM clearly shows that these thick lines are either pairs of dislocations with opposite signs of the Burgers vector, Figs. 15(a) and 15(b), or symmetric oily streaks that separate parts of the very same Grandjean zones, Figs. 15(c) and 15(d). The oily streaks of $b=0$ are most commonly "quadrupoles" composed of two $\lambda^{-1/2}$ and two $\lambda^{+1/2}$ disclinations, sometimes called "Lehmann clusters" [36]. Note that in nonequilibrated freshly prepared samples, the $b=0$ defects can also run parallel to the equilibrium dislocation (y axis) or in some tilted direction.

The $b=0$ lines parallel to the thickness gradient can connect either $b=p/2$ dislocations [Fig. 14(a)], $b=p$ lines [Fig. 14(b)], or one $b=p/2$ and one $b=p$ line [Fig. 14(c)]. The dislocations $b=p/2$ and $b=p$ deviate from the y axis near the node. Deviation of $b=p$ dislocation causes its tilt and a shift to a different z level, which preserves the nonsingular
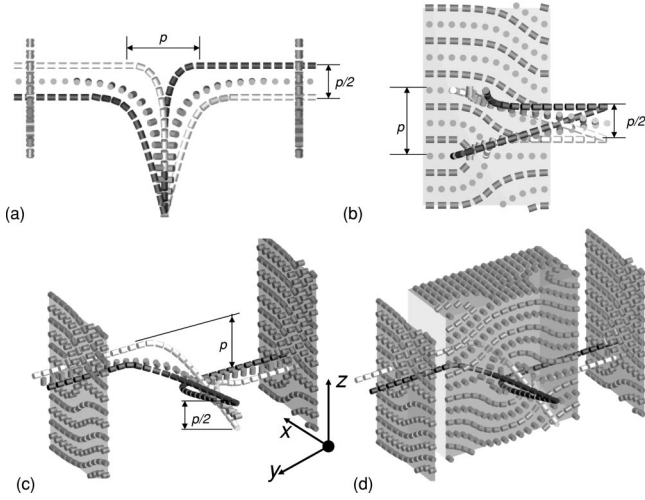
FIG. 12. 3D director field around and at the core of $\lambda^{-1/2}$, $\lambda^{+1/2}$ disclinations in the kink shown in Figs. 9–11, as seen in (a) x-y projection, (b) x-z projection, (c), (d) general 3D prospective.

$\lambda^{-1/2}\lambda^{+1/2}$ geometry of the core, similarly to the kink described in point (2).

In mechanical equilibrium, the sum of line tensions of individual dislocations $\mathbf{T}_i$'s at the dislocation node is zero, $\Sigma_i \mathbf{T}_i = 0$, see, e.g., Ref. [6]. The z shift is small (a fraction of p) as compared to the radius of curvature of the dislocation, so that the z components of $\mathbf{T}_i$'s can be assumed to be much smaller than the x,y components. In this case, mechanical equilibrium dictates $T_0/T_{p/2} = 2\cos\phi_{p/2}$, $T_0/T_p = 2\cos\phi_p$
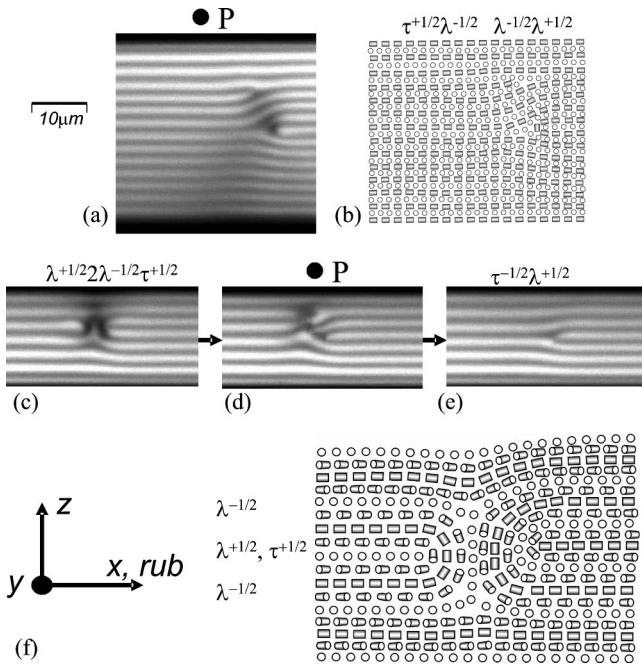

FIG. 13. FCPM vertical cross sections and corresponding director structures of defects with the total Burgers vector $b=p/2$ composed of (a), (b) closely located $\tau^{+1/2}\lambda^{-1/2}$ and $\lambda^{-1/2}\lambda^{+1/2}$ pairs; (c), (d), (e) transformation of the complex core into the $\tau^{-1/2}\lambda^{+1/2}$ pair (e) in the middle of the cell under application of the electric field; (f) shows the director structure in (c).
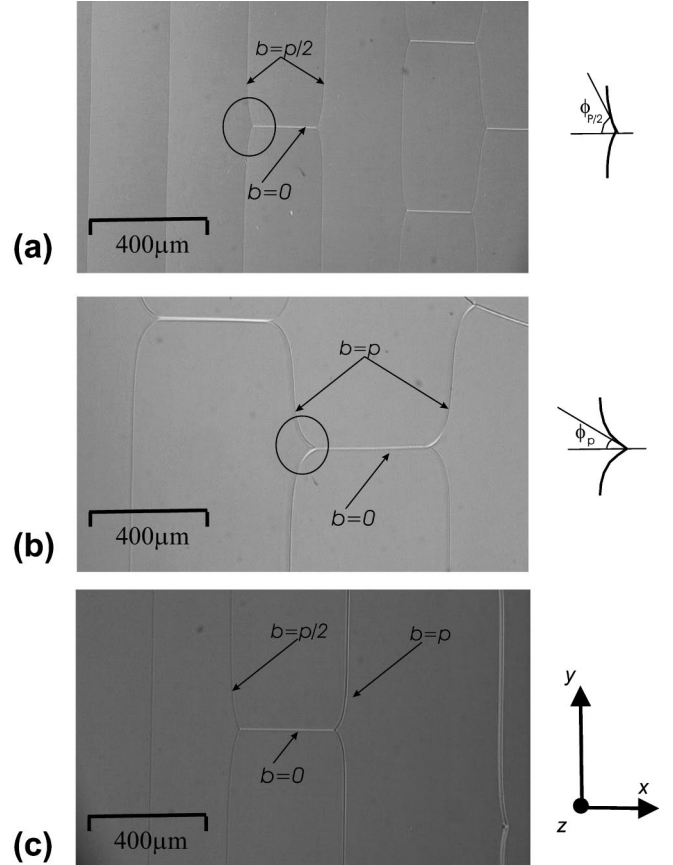

FIG. 14. PM textures of the Grandjean-Cano wedge with defects $b=0$ connecting (a) $b=p/2$; (b) $b=p$; (c) one $b=p/2$ and one $b=p$ dislocations.

and $T_p/T_{p/2} = \cos\phi_{p/2}/\cos\phi_p$; the angles are defined in Fig. 14. Experimentally, $T_0/T_{p/2} \approx 0.7\pm0.2$, $T_0/T_p \approx 1.7\pm0.2$, and $T_p/T_{p/2} \approx 0.4\pm0.2$. The inequality $T_p < T_{p/2}$ is directly related to the split core structures of the defects, as we shall see in the following section.

IV. ELASTICITY OF DEFECT STRUCTURES

In what follows, we construct an elastic model of defect structures in cholesteric Grandjean-Cano wedge. We treat the CLC as a lamellar mesophase and use the Lubensky–de Gennes coarse-grained theory [1,2], in which the free energy density of layers displacements is of the form

$$f_{nl} = \frac{1}{2}K\left(\frac{\partial^2 u}{\partial x^2}\right)^2 + \frac{1}{2}B\left[\frac{\partial u}{\partial z} - \frac{1}{2}\left(\frac{\partial u}{\partial x}\right)^2\right]^2, \quad (1)$$

where the compression elastic modulus $B = K_2(2\pi/p)^2$ and the curvature modulus $K = 3K_3/8$ are related to the Frank moduli of twist (K_2) and bend (K_3), respectively. The two constants define an important "penetration" length $\lambda = \sqrt{K/B}$, that equals $(p/2\pi)\sqrt{3K_3/8K_2}$ in the Lubensky–de Gennes model. Experimental values of λ in CLC with p of the order of few microns are indeed close to the theoretical value $\lambda = (p/2\pi)\sqrt{3K_3/8K_2}$ [37]; for our material with $p = 5$ μm, this theoretical value is $\lambda \approx 0.7$ μm. The contribu-
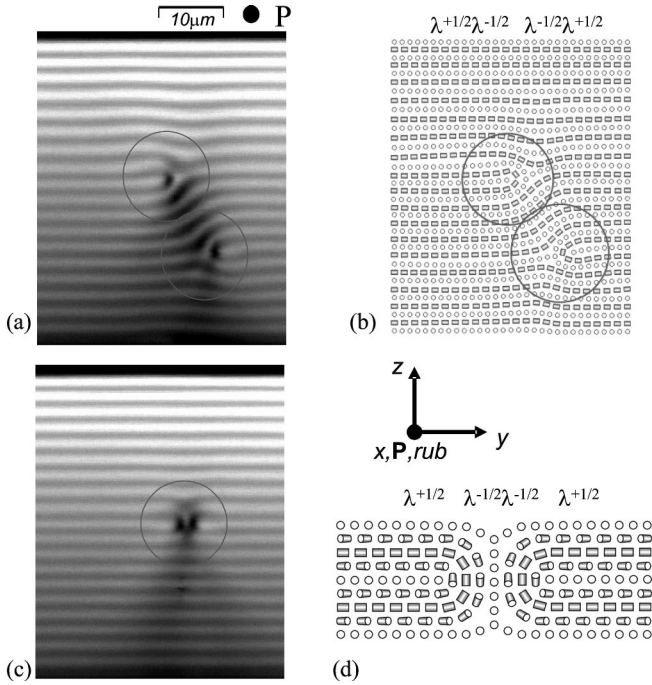
FIG. 15. FCPM vertical cross sections and corresponding director structures of defects with the total Burgers vector $b=0$: (a),(b) two dislocations of $b_1=-b_2=p$ dissociated into $\lambda^{-1/2}$, $\lambda^{+1/2}$ pairs; (c),(d) Lehmann cluster consisting of four λ disclinations.

tion $\frac{1}{2}(\partial u/\partial x)^2$ in the compressibility term in Eq. (1) makes the theory nonlinear; in linear approximation,

$$f_l = \frac{1}{2} K \left(\frac{\partial^2 u}{\partial x^2} \right)^2 + \frac{1}{2} B \left(\frac{\partial u}{\partial z} \right)^2. \quad (2)$$

We consider elastic properties of an isolated edge dislocation first in an infinitely large volume (Sec. IV A), and then in the spatially restricted film, in the approximation of infinitely large surface anchoring (Sec. IV B). We use these results to analyze glide and climb of defects (Sec. IV C) and equilibrium Grandjean-Cano lattice of dislocations (Sec. IV D).

A. Isolated dislocation in an infinitely large sample

Using the nonlinear model, Brener and Marchenko found the equilibrium displacement field around a straight edge dislocation of Burgers vector b in an infinite medium [38]

$$u_{nl}(x,z) = 2\lambda \ln \left\{ 1 + \frac{e^{b/4\lambda}-1}{2} \left[1 + \mathrm{erf}\left(\frac{x}{2\sqrt{\lambda z}} \right) \right] \right\}, \quad (3)$$

where $\mathrm{erf}(\cdots)$ is the error function, defined as $\mathrm{erf}(t) = (2/\sqrt{\pi})\int_0^t \exp(-v^2)dv$; x and z are Cartesian coordinates in the plane perpendicular to the dislocation centered at $(0,0)$. In the limit $b \ll \lambda$, Eq. (3) reduces to the classical result of the linear theory [39,3],

$$u_l(x,z) = \frac{b}{4} \left[1 + \mathrm{erf}\left(\frac{x}{2\sqrt{\lambda z}} \right) \right]. \quad (4)$$

In CLCs, even the smallest value of the Burgers vector, $b = p/2$, is larger than λ and the nonlinear theory is better suited to describe the layer displacement [37]. The nonlinear term in Eq. (1) makes a rigorous analysis of dislocations in CLCs difficult. Fortunately, as shown below, the energies per unit length of edge dislocations calculated in linear and nonlinear models do not differ much for not-so-large values of b/λ ($p/\lambda \approx 7$ in the experiment), and one can employ the linear model for approximate analytical description.

Substituting Eq. (4) in Eq. (2), we calculate the free energy density for an edge dislocation in the linear model,

$$f_{d,l} = \frac{Kb^2 e^{-x^2/2z\lambda} x^2}{64\pi z^3 \lambda^3}. \quad (5)$$

The energy E per unit length L_y of the edge dislocation in a 1D lamellar phase,

$$E = \int_{-\infty}^{\infty} \int_{-\infty}^{\infty} f_{d,l} dz dx = E_{ff} + E_c, \quad (6)$$

is a sum of the "far-field" energy E_{ff} of distortions away from the defect core (in which the cholesteric helicoid is strongly distorted), and the core energy E_c that cannot be determined within the coarse-grained model, as the scale of distortions is p. E_{ff} can be calculated in two ways that differ in the order of integration over x and z.

(a) If the integration is performed first over x in the entire range $(-\infty, \infty)$, then integration over z should be performed in the range $\pm(\xi_z, \infty)$, as one needs to introduce a cutoff length ξ_z near $z \to 0$ to avoid energy divergencies. The result

$$E = 2 \int_{\xi_z}^{\infty} \frac{Kb^2}{32\sqrt{2\pi}\lambda^{3/2}z^{3/2}} dz + E_{z-band} = \frac{Kb^2}{8\sqrt{2\pi\xi_z}\lambda^{3/2}}$$
$$+ E_{z-band} \quad (7)$$

contains the energy E_{z-band} of deformations inside an infinitely long band of width $|z| \leq \xi_z$. In its turn, E_{z-band} can be represented as a sum of the core energy E_c of deformations within a rectangle ($|x| \leq \xi_x, |z| \leq \xi_z$), where ξ_x is some "horizontal" cutoff length, and the energy of two bands ($\xi_x \leq |x| < \infty, |z| \leq \xi_z$) in which the deformations are relatively weak:

$$E_{z-band} = 2 \int_{-\xi_z}^{\xi_z} dz \int_{\xi_x}^{\infty} f_{d,l} dz + E_c = \frac{Kb^2}{8\sqrt{2\pi\xi_z}\lambda^{3/2}}$$
$$\times \left[-1 + \sqrt{\frac{2}{\pi\beta}} \exp(-2\beta) + \mathrm{erf}\sqrt{2\beta} \right] + E_c, \quad (8)$$

where $\beta = \xi_x^2/(4\lambda\xi_z)$.

(b) With the reverse order of integration, the cutoff length ξ_x (generally *different* from ξ_z), is introduced first along the x axis,

$$E = 2 \int_{\xi_x}^{\infty} \frac{Kb^2}{8\pi\lambda x^2} dx + E_{x-band} = \frac{Kb^2}{4\pi\xi_x\lambda} + E_{x-band}, \quad (9)$$

where E_{x-band} is the energy of deformations within the infinitely long band $|x| \leqslant \xi_x$,

$$E_{x-band} = 2 \int_{-\xi_x}^{\xi_x} dx \int_{\xi_z}^{\infty} f_d dz + E_c$$

$$= \frac{Kb^2}{4\pi\xi_x\lambda} \left[-1 + \exp(-2\beta) + \sqrt{\frac{\pi\beta}{2}} \, \text{erf}\sqrt{2\beta} \right] + E_c.$$

(10)

Therefore, the far-field energy E_{ff} can be written in two equivalent forms,

$$E_{ff} = \frac{Kb^2}{8\sqrt{2\pi\xi_z}\lambda^{3/2}} \left[\sqrt{\frac{2}{\pi\beta}} \exp(-2\beta) + \text{erf} \sqrt{2\beta} \right]$$

$$\equiv \frac{Kb^2}{4\pi\xi_x\lambda} \left[\exp(-2\beta) + \sqrt{\frac{\pi\beta}{2}} \text{erf} \sqrt{2\beta} \right].$$

(11)

Note that the relationship between the two forms is that of identity type and cannot be used to determine the core parameter $\beta = \xi_x^2/(4\lambda\xi_z)$.

The far-field energy E_{ff} derived above depends on two core sizes ξ_x and ξ_z along the two axes x and z, rather than on one as in the classic Kleman model [3], in which the far-field energy has been calculated outside a stripe $|x| \leqslant \xi_x$, $-\infty < z < \infty$. The two quantities ξ_x and ξ_z might be related in a nontrivial way, depending on λ and b; their values cannot be established on the basis of the coarse-grained model. If one assumes $\xi_x^2 = 4\lambda\xi_z$, following the idea that perturbation of length δ_x along the layers propagates over the distance $\delta_z \sim \delta_x^2/(4\lambda)$ along the z axis, then $\beta = 1$, and

$$E_{ff} \approx 1.06 \frac{Kb^2}{8\sqrt{2\pi\xi_z}\lambda^{3/2}} \approx 1.33 \frac{Kb^2}{4\pi\xi_x\lambda} \approx \frac{Kb^2}{3\pi\xi_x\lambda}. \quad (12)$$

Furthermore, if $\xi_x^2 \gg 4\lambda\xi_z$, $\beta \to \infty$, then $[\sqrt{2/(\pi\beta)} \exp(-2\beta) + \text{erf} \sqrt{2\beta}] \to 1$ and $E_{ff} = Kb^2/(8\sqrt{2\pi\xi_z}\lambda^{3/2})$; if $\xi_x^2 \ll 4\lambda\xi_z$, $\beta \to 0$, then $[\exp(-2\beta) + \sqrt{\pi\beta/2} \, \text{erf} \sqrt{2\beta}] \to 1$ and $E_{ff} = Kb^2/(4\pi\xi_x\lambda)$. Note that the leading term $E_{ff} = Kb^2/(4\pi\xi_x\lambda)$ in the far-field energy (11) transforms into the result derived by Kleman [3], $E_{ff} = Kb^2/(2\xi_x\lambda)$, with a rescaled cutoff radius $2\pi\xi_x \to \xi_x$.

The function $E_{ff}(b)$, formally quadratic in Eq. (11), is in fact dependent on the model of the dislocation core. As suggested by Kleman [3], if the dislocation core is split into a pair of disclinations, then the horizontal cutoff ξ_x scales as b; roughly, $\xi_x \approx b/2$; at the same time ξ_z, being a distance along the z-axis, at which the semiwidth x of the parabolas $x^2 = 4\lambda z$ reaches $p/2$, is taken as independent of b. With $\xi_x \approx b/2$, the far-field energy $E_{ff} \approx Kb^2/(3\pi\xi_x\lambda) \approx 2Kb/(3\pi\lambda)$ is a linear function of b; the result implies that dislocations with large Burgers vector are stable against splitting into two or more dislocations with smaller b's.

Following the same procedure with Eqs. (1) and (3), we numerically calculate the difference $E_{ff} = E - E_c$ of the edge dislocation in the framework of nonlinear theory. In the range of $b/\lambda = 1-8$, with the same cutoff parameters $\xi_x = b/2$ and $\beta = 1$, the difference between the linear and nonlinear results is small, within 2% of E_{ff}; uncertainties in core energies E_c are expected to be much larger. In the experiment, the largest value of $b/\lambda = p/\lambda$ is about 7, so that we can use the linear approximation for further analysis.

The experiments clearly show that the dislocation cores are split into pairs of disclinations. The core energy of the split dislocations is estimated [3] as a sum $E_c(b) = E_{pair}(b) + E_c'$ of (I) the energy $E_{pair}(b)$ of a pair of disclinations separated by distance $2\xi_x \sim b/2$; (II) core energy E_c' of the disclination lines themselves; this quantity depends little on b, but is extremely sensitive to whether the disclination is singular (large E_c') or not (small E_c'). As compared to the $\lambda^{-1/2}\lambda^{+1/2}$ pair, the core energy of the $\tau^{-1/2}\lambda^{+1/2}$ pair should contain an additional term $\sim K \ln(p/r_c)$ that reflects the singular nature of $\tau^{-1/2}$ disclination with the core size r_c of the order of 1–10 molecular sizes [5].

For the $\tau^{-1/2}\lambda^{+1/2}$ pair, integrating the typical distortion energy density, $\frac{1}{2}(K/r^2)$, between $r = r_c$ and $r = b/2 = p/4$, one obtains

$$E_{c,\tau\lambda} = E_{pair} + E_c' \approx \frac{\pi}{2} K \ln\left(\frac{p}{4r_c}\right) + C_1 K, \quad (13)$$

where C_1 is a number of the order of unity. E_c' should not differ much from the estimate $E_c' = C_1 K = (\pi/8)K$ suggested by Oswald and Pieranski [21] for the singular core of a nematic disclination of winding number $\pm 1/2$, which implies $C_1 = \pi/8 \approx 0.4$. For typical $p \approx 5$ μm and $r_c \approx 5$ nm, the logarithmic factor in Eq. (13) is relatively large, $\ln(p/4r_c) \approx 6$.

In the core of dislocation $b = p$ split into a $\lambda^{-1/2}\lambda^{+1/2}$ pair, the twist structure is distorted over the area $\sim p^2$, and the core energy is roughly

$$E_{c,\lambda\lambda} = C_2 K, \quad (14)$$

where C_2 is another number of the order of unity; therefore, one expects $E_{c,\lambda\lambda}$ to be about one order of magnitude smaller than $E_{c,\tau\lambda}$ when $p \approx 5$ μm and $r_c \approx 5$ nm.

Remember that the quantities $E_{c,\tau\lambda}$, $E_{c,\lambda\lambda}$ and thus E considered above are elastic energies per unit length of the defect but *not* the line tensions of defects. The line tension T, defined as the ratio of the variation of elastic energy $\delta E = T\delta l$ to the variation in its length δl, depends on the orientation of edge dislocation in the cholesteric matrix, $T \approx [E(\gamma) + \partial^2 E(\gamma)/\partial\gamma^2]_{\gamma=0}$, where γ is the angular deviation of dislocation from the y axis (see, e.g., Ref. [6], Chaps. 8 and 9). If the dislocation stays in the same x-y plane, then reorientation implies a change in the core structure. For example, $\gamma = \pi/2$ transforms $\tau^{-1/2}\lambda^{+1/2}$ into $\lambda^{-1/2}\tau^{+1/2}$ and $\lambda^{-1/2}\lambda^{+1/2}$ into $\tau^{-1/2}\tau^{+1/2}$, with a corresponding energy increase that is especially pronounced in the second case. Estimating the core energy increase under the transformation $\lambda^{-1/2}\lambda^{+1/2} \to \tau^{-1/2}\tau^{+1/2}$ as $(\pi/2)K \ln(p/2r_c)$, one finds the core contribution to the line tension of $\lambda^{-1/2}\lambda^{+1/2}$ pair curved in the same x-y plane as $E_{c,\lambda\lambda} + \pi K \ln(p/2r_c) \gg E_{c,\lambda\lambda}$. A curved dislocation line thus should experience a

torque tending to deviate it from the x-y plane, i.e., to avoid the singular $\tau^{-1/2}\tau^{+1/2}$ core. The same mechanism is responsible for the geometry of kinks along the $b=p$ dislocations, Fig. 12.

As the $\lambda^{-1/2}\lambda^{+1/2}$ dislocations preserve their core structure upon deviations from the y-axis and shift along the z axis, their actual line tension is close to the energy per unit length, i.e, $T_p \approx E_{ff}(b=p) + E_{c,\lambda\lambda} \approx 2Kp/(3\pi\lambda) + C_2 K$ or $T_p \approx 3K$ when $C_2 \approx 1$. For the $b=p/2$ dislocation, one of the disclinations in the core remains always singular, thus the rough estimate of its line tension is $T_{p/2} \approx E_{ff}(b=p/2) + E_{c,\tau\lambda} \approx Kp/(3\pi\lambda) + (\pi/2)K \ln(p/4r_c) + C_1 K \approx 10$ K with the parameters specified above. Therefore, $T_p/T_{p/2} \approx 0.3$, comparable to the experimental value 0.4 ± 0.2.

Why then $b=p/2$ dislocations with a very large core energy appear in the thin part of sample? Qualitatively, the reason is that inserting a slab of thickness $b=p/2$ into the wedge requires less compression energy as compared to a slab of thickness $b=p$. Obviously, the difference is significant only when the number N of layers in the wedge is small, and gradually decreases with an increase of N. Therefore, dislocations $b=p/2$ should be replaced by $b=p$ dislocations at $h>h_c$. We discuss the stability of $b=p/2$ versus $b=p$ dislocations and h_c in a greater detail in Sec. IV D.

B. Isolated dislocation in a confined sample

The bounding surfaces can dramatically change layer profiles and other properties of dislocations. So far, the effect has been studied for thermotropic smectic liquid crystal and block copolymer samples with a free surface, in which case the relevant factor is a finite surface tension [19,40–42]. If the coefficient of surface tension is large, $\sigma > \sqrt{KB}$, the dislocation is pushed away from the bounding surface. In Grandjean-Cano wedges bounded by rigid glass plates, the relevant factor is surface anchoring, which is sufficiently strong to keep the dislocations in the bulk. The cholesteric layers adjacent to the glass plates, Figs. 4, 7–10, are practically (but not exactly) parallel to the substrates $z = \pm h/2$, i.e., one can assume $\partial u/\partial x|_{z=\pm h/2} = 0$. The layers displacement around a dislocation centered at $z=0$ can be modeled by placing an infinite set of image dislocations outside the sample, at $z = \pm mh$, $m = 1,2,3, \ldots$; their Burgers vectors equal that of the real dislocation b [43]. To estimate the effects of confinement on the dislocation energy, we consider only the first two images closest to the substrates. In the linear model, the displacement field $u_{conf}(x,z)$ of a confined dislocation is a superposition of displacements caused by the defect and its images,

$$u_{conf}(x,z) \simeq \frac{b}{4} \sum_{m=-1,0,1} \frac{z+mh}{|z+mh|} \left[1 + \mathrm{erf}\left(\frac{x}{2\sqrt{\lambda|z+mh|}} \right) \right].$$
(15)

Proceeding as above for an unbounded dislocation, one can calculate the energy E_{conf} (per unit length) of the bounded dislocation, $E_{conf} = 2\int_0^{h/2} dz \int_{-\infty}^{\infty} f_{d,l}[u_{conf}(x,z)]dx = E_{ff} + E_h + E_{z\text{-}band}$, where E_h is the correction to the far-

field energy caused by confinement. In the limit $\xi_z/h \ll 1$, the leading term of the confinement correction is

$$E_h \approx -\frac{Kb^2}{8\sqrt{2\pi\xi_z}\lambda^{3/2}} \left(\frac{5}{2\sqrt{2}} + \frac{1}{\sqrt{3}} - 1 \right) \sqrt{\frac{2\xi_z}{h}}$$

$$\approx -\frac{Kb^2}{4\sqrt{2\pi h}\lambda^{3/2}}.$$
(16)

The correction is significant only for relatively thin samples, for example, $E_h \approx -0.4E_{ff}$ for $\xi_z/h = 0.1$. As $E_h \sim b^2$, image forces in a strongly anchored sample facilitate splitting of dislocations into defects with a smaller b. Finally, we keep the core energies E_c the same as above; as long as the dislocations are not very close to the boundaries, their core structures are h independent, as confirmed by FCPM observations.

C. Peach and Koehler forces on edge dislocations

Location of dislocations in a confined sample can be analyzed in terms of configurational (Peach and Koehler) force [6],

$$\mathcal{F}_i^E = \varepsilon_{ijk} b_l \sigma_{lj}^E t_k,$$
(17)

where ε_{ijk} is the Levi-Chivita tensor, $\mathbf{t}$ is the unit vector along the dislocation line, $\boldsymbol{\sigma}^E$ is the elastic stress tensor, related to the layer displacements caused by stresses other than that of the dislocation under consideration. In the linear approximation, the nonvanishing stress tensor components relevant to the 2D case $u=u(x,z)$ are

$$\sigma_{zz}^E = B\frac{\partial u}{\partial z}, \quad \sigma_{zx}^E = -K\frac{\partial^3 u}{\partial x^3}.$$
(18)

For an edge dislocation with $\mathbf{b} = b(0,0,1)$ and $\mathbf{t} = (0,1,0)$,

$$\mathcal{F}_x^E = -\sigma_{zz}^E b = Bb\frac{\partial u}{\partial z}, \quad \mathcal{F}_y^E = 0, \quad \mathcal{F}_z^E = \sigma_{zx}^E b = -Kb\frac{\partial^3 u}{\partial x^3}.$$
(19)

1. Climb

Let a dislocation be located at x_d', where x' is measured from the end of the wedge; x_{de}' is a position of equilibrium, Fig. 1. To simplify the notations, in this section we use the coordinate system (x',z'), in which the x' axis is directed along the bottom plate; this plate is located at $z'=0$. Dislocations at equilibrium separate the regions of compression and dilation of layers. The stress σ_{zz}^E vanishes at $x'=x_{de}'$ and at some location between two neighboring dislocations, where the thickness of the wedge is $h_N = Np/2$; N is an integer. To find x_{de}', we calculate the B term in Eq. (2) in a part of the wedge of length $b/\tan\alpha$, and height h_N on the left side and $h_N + b$ on the right side:

$$E_B(x_d) = \frac{B}{2}\left[\int_{h_N/\tan\alpha}^{x'_d} dx \int_0^{x\tan\alpha}\left(\frac{\partial u^-}{\partial z}\right)^2 dz\right.$$

$$\left. + \int_{x'_d}^{(h_N+b)/\tan\alpha} dx \int_0^{x\tan\alpha}\left(\frac{\partial u^+}{\partial z}\right)^2 dz\right]. \quad (20)$$

Here, $\partial u^-/\partial z = x\tan\alpha/h_N - 1$ and $\partial u^+/\partial z = x\tan\alpha/(h_N+b) - 1$. The energy is minimized, $\partial F_B(x'_d)/\partial x'_d = 0$, when the dislocation is in the equilibrium position

$$x'_{de}(N) = \frac{2h_N(h_N+b)}{(2h_N+b)\tan\alpha} = \frac{Np(Np+2b)}{2(Np+b)\tan\alpha}. \quad (21)$$

The same result follows from a direct calculation of the Peach-Koehler force, $\mathcal{F}_x^E = -Bb(\partial u^-/\partial z + \partial u^+/\partial z)|_{x'_d}$ that vanishes at $x'_d = x'_{de}$. The distances between two neighboring dislocations at equilibrium are

$$l = \frac{2(N+1)^2 p}{(2N+1)(2N+3)\tan\alpha}, \quad L = \frac{(N+2)^2 p}{(N+1)(N+3)\tan\alpha} \quad (22)$$

for $b=p/2$ and $b=p$ types, respectively; here N refers to the number of cholesteric layers $p/2$ to the left of the dislocation located in the thinner part of the wedge. The separation is a weak function of N; it quickly approaches $b/\tan\alpha$ when $N \rightarrow\infty$; even for N as small as 5, the relative difference between $b/\tan\alpha$ and the exact separating distances in Eq. (22) are negligible, less than 2%. In the well-equilibrated samples, dislocations are indeed close to their locations specified by Eq. (21) with separations as in Eq. (22).

A dislocation slightly shifted from its equilibrium position along the x' axis, by $\delta_x = x'_d - x'_{de}$, $|\delta_x| \ll b/2\alpha$, experiences a restoring force $\mathcal{F}_x^E(\delta_x) = -\sigma_{zz}^E b = -\partial E_B(x'_{de}+\delta_x)/\partial\delta_x$ with the direction opposite to the direction of δ_x,

$$\mathcal{F}_x^E(\delta_x) \approx -\frac{Bb\,\delta_x\tan\alpha}{h_N}\frac{2h_N+b}{2(h_N+b)}; \quad (23)$$

this force causes dislocation to climbing back to $x'=x'_{de}$. Note here that climb parallel to the layers is easier than glide across the layers, as it preserves the essential geometry of the core and is associated with twist deformations near the core. Because the stresses imposed by the wedge geometry are thickness dependent and small, and because real-time FCPM experiments at this stage are difficult, we leave the discussion of the mobility of dislocations to a future study.

2. Glide

Consider now a case when the dislocation is shifted along the vertical z axis from $z=0$ to some $\delta_z \neq 0$. Here we return to the coordinate system with the x axis along the midplane of the wedge. Because of the boundary conditions $\partial u/\partial x|_{z=\pm h/2} = 0$, the dislocation is repelled by the boundary towards the midplane. The corresponding Peach-Koehler force $\mathcal{F}_z^E(z_d) = b\sigma_{zx}^E|_{z=\delta_z}$ can be calculated by placing image dislocations of the same Burgers vector b at both sides of the slab, $z=-mh+(-1)^m\delta_z$ and $z=mh+(-1)^m\delta_z$ [43],

where $m=1,2,\ldots,\infty$. The neighboring dislocations to the left and to the right can be neglected, as long as the dihedral angle α and the cell thickness are sufficiently small so that the parabolic regions $x^2 \leq 4\lambda|z|$ of layers distortions around neighboring dislocations do not overlap. In the linear approximation, the displacement field u_{zi} caused by the image dislocations is

$$u_{zi}(x,z) = \frac{b}{4}\sum_{m=1}^{\infty}\left[\text{erf}\left(\frac{x}{2\sqrt{\lambda(mh-(-1)^m\delta_z+z)}}\right)\right.$$

$$\left. -\text{erf}\left(\frac{x}{2\sqrt{\lambda(mh+(-1)^m\delta_z-z)}}\right)\right]. \quad (24)$$

The repelling force $\mathcal{F}_z^E(\delta_z) = -bK(\partial^3 u_{zi}/\partial x^3)|_{z=\delta_z;x=0}$ is then [43]

$$\mathcal{F}_z^E(\delta_z) = \frac{Kb^2}{8\sqrt{\pi}\lambda^{3/2}h^{3/2}}\sum_{m=1.}^{\infty}\left\{\left[m+\frac{\delta_z}{h}[1-(-1)^m]\right]^{-3/2}\right.$$

$$\left. -\left[m-\frac{\delta_z}{h}[1-(-1)^m]\right]^{-3/2}\right\}. \quad (25)$$

The force vanishes for $\delta_z=0$. When the displacements from the middle plane are small, $\delta_z \ll h$, series expansion and summation on the right hand part of the last equation yield a simple formula for the force,

$$\mathcal{F}_z^E(\delta_z) \approx -\frac{3(8-\sqrt{2})}{4}\varsigma\left(\frac{5}{2}\right)\frac{Kb^2}{8\sqrt{\pi}\lambda^{3/2}h^{3/2}}\frac{\delta_z}{h}+O\left(\frac{\delta_z^3}{h^3}\right)$$

$$\approx -\frac{0.47Kb^2}{\lambda^{3/2}h^{3/2}}\frac{\delta_z}{h}, \quad (26)$$

where $\varsigma(\cdots)$ is the Riemann zeta function, and stress,

$$\sigma_{zx}^E(\delta_z) \approx \frac{0.47Kb}{\lambda^{3/2}h^{3/2}}\frac{\delta_z}{h}. \quad (27)$$

The force $\mathcal{F}_z^E(\delta_z)$ is always directed to drive the dislocation to the midplane of a strongly-anchored wedge; this force quickly decreases when the thickness of the slab increases, $\mathcal{F}_z^E \sim h^{-5/2}$.

We recall now that in the experiments, $b=p$ dislocations are often found away from the bisector plane, while $b=p/2$ dislocations are close to it. The apparent discrepancy with the model prediction $\mathcal{F}_z^E(\delta_z) \sim b^2$ is explained by the fact that glide of dislocations is hindered by periodic structure of the cholesteric.

In solid-state physics, the phenomenon is known as the Peierls-Nabarro friction [44,45]. As the dislocation glides across the crystal lattice, the core structure changes periodically; atomic reconstructions lead to periodic changes of the potential energy of the crystal. The applied stress needed to overcome the energy barriers is called the Peierls-Nabarro stress. This stress is determined by the core structure and thus cannot be given a universal analytical expression. The
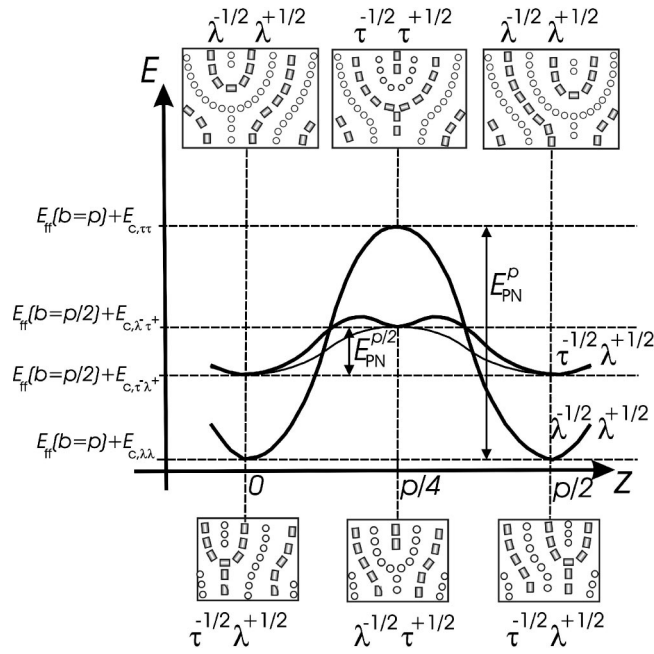
FIG. 16. Potential energies of straight dislocations $b=p/2$ and dislocation $b=p$ with the split cores as the functions of their position aling the z axis; see text.

original Peierls-Nabarro model assumes a sinusoidal force between the atomic planes on the two sides of the slip plane. Lejcek [46] has applied the model to edge dislocations in Sm-A and calculated the Peierls-Nabarro stress that reads in our notations as

$$\sigma_{PNL} \approx \frac{3\sqrt{\pi}Kb}{4\lambda^{3/2}\xi_z^{1/2}} \exp\left(-\frac{2\pi\xi_z}{b}\right). \qquad (28)$$

It is easy to see that the ratio

$$\frac{\sigma_{PNL}}{\sigma_{zx}^E} \approx \frac{3\sqrt{\pi}}{2\exp(2\pi\xi_z/b)} \frac{h^{5/2}}{b\xi_z^{1/2}\delta_z}$$

can be of the order of 1 with estimates $b=\delta_z=\xi_z=p$, $\lambda=0.2p$, $h=10p$. The ratio $\sigma_{PNL}/\sigma_{zx}^E$ decreases when h decreases, which, in principle, might explain the fact that $b=p/2$ dislocations in the thin part of the sample are located near the bisector plane, while the $b=p$ lines in the thick part are found at different z levels. Note, however, that the steep dependence of σ_{PNL} on the model core parameter ξ_z makes the estimates rough. Moreover, the model (28) refers to a dislocation that is not split into a pair of disclinations. Below, we discuss the Peierls-Nabarro stress for the split dislocation and show that the dependence of the split core energy on the position along the helix axis might lead to Peierls-Nabarro stresses higher than σ_{PNL}.

When an edge dislocation with a split core moves as a whole in z direction, the structure of the two disclinations changes periodically. Upon a shift by $p/4$, the pair $\lambda^{-1/2}\lambda^{+1/2}$ transforms into $\tau^{-1/2}\tau^{+1/2}$ and the pair $\tau^{-1/2}\lambda^{+1/2}$ transforms into $\lambda^{-1/2}\tau^{+1/2}$, Fig. 16. The main contribution to the energy changes comes from the energy of the cores; the

far-field energy can be assumed constant. As discussed above, the core energy of the $\lambda^{-1/2}\lambda^{+1/2}$ pair is relatively small, $E_{c,\lambda\lambda}=C_2K\sim K$, Eq. (14). The transformation $\lambda^{-1/2}\lambda^{+1/2}\to\tau^{-1/2}\tau^{+1/2}$ implies a large increase in the core energy, of the order of $E_{PN}^p\approx E_{c,\tau\tau}-E_{c,\lambda\lambda}\approx K\ln(p/r_c)\gg E_{c,\lambda\lambda}$. In contrast, the minimum core energy of the $\tau^{-1/2}\lambda^{+1/2}$ pair is already large, $E_{c,\tau\lambda}\approx(\pi/2)K\ln(p/4r_c)+C_1K$, according to Eq. (13), see Fig. 16. The alternative $\lambda^{-1/2}\tau^{+1/2}$ core apparently corresponds to a local minimum in the potential energy as one does observe kinks that transform $\tau^{-1/2}\lambda^{+1/2}$ into $\lambda^{-1/2}\tau^{+1/2}$ and back, Fig. 7. The transformation $\tau^{-1/2}\lambda^{+1/2}\to\lambda^{-1/2}\tau^{+1/2}$ implies an increase in the core energy by $E_{PN}^{p/2}\approx(\pi/2)K\ln(r_c/r_c')+(C_1'-C_1)K\approx cK$, where primed values correspond to the pair $\lambda^{-1/2}\tau^{+1/2}$; the numerical constant c is most probably less than 1 (an estimate is given at the end of this section).

The excess free energy as the function of dislocation displacement δ_z along the helix axis can be written phenomenologically as

$$\Delta E(\delta_z) \approx \frac{E_{PN}}{2}\left(1-\cos\frac{4\pi b}{p}\frac{\delta_z}{b}\right) = E_{PN}\sin^2\frac{2\pi\delta_z}{p}, \qquad (29)$$

similarly to the phenomenological model for solid crystals [44,45]; E_{PN} is the Peierls-Nabarro energy, Fig. 16. Note that we approximate the two-minima potential for the $\tau^{-1/2}\lambda^{+1/2}$ pair with a single-minimum cosinusoidal function, shown by a thin line in Fig. 16. The corresponding stress

$$\frac{1}{b^2}\frac{\partial\Delta E(\delta_z/b)}{\partial(\delta_z/b)} = \frac{2\pi E_{PN}}{pb}\sin\left(\frac{4\pi\delta_z}{p}\right)$$

has the amplitude $\sigma_{PNcore}=2\pi E_{PN}/(pb)$, or, when written for the two types of dislocations separately,

$$\sigma_{PNcore}^p \approx \frac{2\pi K\ln\left(\dfrac{p}{r_c}\right)}{pb}, \quad \sigma_{PNcore}^{p/2}\approx\frac{2\pi cK}{pb}. \qquad (30)$$

For the $\lambda^{-1/2}\lambda^{+1/2}$ pair, with $b=\delta_z=p$, $\lambda=0.2p$, $h=10p,p\approx5$ μm, and $r_c\approx5$ nm, one finds $\sigma_{zx}^E/\sigma_{PNcore}^p\approx4\times10^6$; therefore, the model predicts that $\lambda^{-1/2}\lambda^{+1/2}$ pair cannot glide as a straight line. For the $\tau^{-1/2}\lambda^{+1/2}$ pair, with $b=\delta_z=p/2$, $\lambda=0.2p$, $h=10p$, one finds $\sigma_{zx}^E/\sigma_{PNcore}^{p/2}\approx4\times10^5c$; unless c is anomalously small (as estimated below, c is of the order of 10^{-2}), the Peierls-Nabarro barrier is too high to allow the dislocation $b=p/2$ to glide as well.

The considerations above are in a good agreement with the experimental data. We have never observed glide of dislocations as a whole. Instead, the change in z coordinate occurs via kinks. The kinks have completely different structure for the case of $b=p/2$ and $b=p$ dislocations, as presented in the experimental part and discussed below.

The kinks that occur along the $b=p/2$ dislocations are usually of height $p/4$ or $p/2$ each, Figs. 7 and 8. The length of the kink, measured along the y axis, is large, $w\sim(5-10)$ p, i.e., the angle ψ between the kink and the y axis is small.

This experimental feature indicates that the Peierls-Nabarro energy barrier is relatively small as compared to the line tension of the dislocation itself. Imagine a dislocation connecting two points in the bulk of the sample, $A(x_A, z_A)$ and $B(x_B, z_B)$. The smaller the Peierls-Nabarro energy as compared to the line energy of the dislocation, the smaller is ψ: in the limiting case $E_{PN}/E \to 0$, the kink is infinitely long, as the dislocation simply tilts as a whole and preserves the form of a straight line to minimize its length $\sqrt{(x_B - x_A)^2 + (z_B - z_A)^2}$. When the Peierls-Nabarro energy associated with the kink is larger than the line tension, then ψ is large and the kink tends to be short; in the limit $E_{PN}/E \to \infty$, the kink is vertical, of the length $|z_B - z_A|$, it connects two horizontal dislocation segments of total length $|x_B - x_A|$.

For small ψ, one can directly apply the kink model developed for solid crystals [44,45], in which ψ is determined by the (constant) line tension of the edge dislocation $E_{p/2} \approx E_{c,\tau\lambda} \approx (\pi/2)K \ln(p/4r_c)$, Eq. (13), and the Peierls-Nabarro energy $E_{PN}^{p/2} \approx cK$, as $\psi = \sqrt{2E_{PN}^{p/2}/E_{p/2}}$. As $\psi = p/(4w)$ for the $p/4$ kink, one obtains

$$w \approx \frac{p}{4}\sqrt{\frac{E_{p/2}}{2E_{PN}^{p/2}}} \approx \frac{p}{4}\sqrt{\frac{\pi}{4c}\ln\frac{p}{4r_c}}.$$

Using the estimates $p \approx 5$ μm and $r_c \approx 5$ nm, and the experimental result $w \sim (5\text{--}10)p$, one obtains $c \sim (0.3\text{--}1) \times 10^{-2}$. In other words, the core energy variation for the $\tau^{-1/2}\lambda^{+1/2}$ pair along the kink is only a small fraction of the Frank elastic constant K, which is a reasonable conclusion as the $b = p/2$ dislocation can never get rid of the singular core.

In contrast, for a kink along the $b = p$ dislocation, the $\lambda^{-1/2}\lambda^{+1/2}$ pair simply twists with the local cholesteric director to preserve the nonsingular core, Fig. 12; the energy density of the kink is of the order of K and is not very different from the line tension $E_p \sim K$ of the dislocation itself; therefore, the kinks are expected to be short, $w \sim p$, as in the experiments.

Note also that the total elastic energy U of the kinks in cholesterics with a micron-scale pitch is expected to be much larger than the thermal energy ($k_B T \approx 4 \times 10^{-21}$ J at room temperature), which makes their thermal nucleation unlikely; the situation is thus different from the typical Sm-A materials, in which the kinks are mostly of molecular height. For the kinks along the cholesteric $b = p$ dislocation, the discussion above leads to $U_p \sim (K/p^2)p^3 \sim pK \sim 5 \times 10^{-17}$ J. For the "long" kinks along the $b = p/2$ dislocation, the energy is $U_{b/2} \sim E_{p/2}b^2/w$, i.e., $U_{b/2} \sim (\pi/2)Kp^2 \ln(p/4r_c)/(4w) \sim 10^{-17}$ J. The observed kinks can be introduced during the filling of the samples and by mechanical inhomogeneities, including the edges of the cholesteric sample.

D. Lattice of dislocation in an equilibrated confined sample: Critical thickness

We follow the approach of Nallet and Prost [22], in which the energy of the wedge is represented as the sum of the independent compression/dilation energy E_B and the energy of dislocations. The strain field due to the presence of dislo-

cation is significant only within the parabola $x^2 = 4\lambda|z|$. In the wedge of small angle α, the dislocations are separated by distances $l \geqslant 2\sqrt{4\lambda h}$ and practically do not interact. Therefore, the free energy per unit length in y direction can be represented as a sum $E = E_B + F_{ff} + E_h + E_{core}$, where E_B is the B term energy of the type (20), E_{ff} is the far-field energy due to the strain field inside the parabolae (5), E_h is the correction to the far-field energy that accounts for confinement effects (16), and E_{core} is the core energy (14) or (13). The defects are in their equilibrium positions $x'_{de}(N)$, Eq. (21), in the bisector plane; x' axis is along the bottom plate. We compare the energies of the two types of lattices: one with $b = p/2$ and one with $b = p$. Calculations are performed for a trapezium of length $b/\tan\alpha$ and height h_N on the left side and $h_N + p$ on the right side. The trapezium contains either two dislocations with $b = p/2$ or one with $b = p$.

The B term is calculated using the symmetry of the stress σ_{zz}^E that vanishes at $x' = x'_{de}(N)$ and at any location of the type $h_N = Np/2$ between dislocations. For the lattice composed of $b = p$ dislocations,

$$
\begin{aligned}
E_B^p &= B/2\Bigg[\int_{h_N/\tan\alpha}^{x'_{de}(N, b=p)} dx \int_0^{x\tan\alpha} (x\tan\alpha/h_N - 1)^2 dz \\
&\quad + \int_{x'_{de}(N, b=p)}^{(h_N+p)/\tan\alpha} dx \int_0^{x\tan\alpha} (x\tan\alpha/h_N + p - 1)^2 dz \Bigg] \\
&= \frac{Bp^2}{24\tan\alpha}\frac{2N^2 + 4N + 1}{[1+N]^3} \\
&\approx \frac{Bp^2}{12\tan\alpha}\left(\frac{1}{N} - \frac{1}{N^2}\right).
\end{aligned} \tag{31}
$$

In a similar way, for the $b = p/2$ dislocations,

$$
\begin{aligned}
E_B^{p/2} &= B/2\Bigg[\int_{h_N/\tan\alpha}^{x'_{de}(N, b=p/2)} dx \int_0^{x\tan\alpha} (x\tan\alpha/h_N - 1)^2 dz \\
&\quad + \int_{x'_{de}(N, b=p/2)}^{x'_{de}(N+1, b=p/2)} dx \int_0^{x\tan\alpha} (x\tan\alpha/h_N + p/2 - 1)^2 dz \\
&\quad + \int_{x'_{de}(N+1, b=p/2)}^{(h_N+p)/\tan\alpha} dx \int_0^{x\tan\alpha} (x\tan\alpha h_N + p - 1)^2 dz \Bigg] \\
&= \frac{Bp^2}{24\tan\alpha}\frac{32N^5 + 160N^4 + 300N^3 + 260N^2 + 99N + 11}{[4N^2 + 8N + 3]^3} \\
&\approx \frac{Bp^2}{48\tan\alpha}\left(\frac{1}{N} - \frac{1}{N^2}\right).
\end{aligned} \tag{32}
$$

The far-field energy of dislocation with $\xi_x = b/2$ is $E_{ff} \approx 2Kb/(3\pi\lambda)$, Eq. (12); the confinement correction is roughly $E_h \approx -Kb^2/(4\sqrt{2\pi h}\lambda^{3/2}) \approx -Kb^2/(4\sqrt{\pi Np}\lambda^{3/2})$, Eq. (16); and the core energies are specified either as $E_{c,\tau\lambda} \approx (\pi/2)K \ln(p/4r_c) + C_1 K$, Eq. (13) or as $E_{c,\lambda\lambda} = C_2 K$, Eq.

(14), depending on the dislocation type. Therefore, the total elastic energies of the two structures are

$$\frac{E_{p/2}}{K} \approx \frac{p^2}{48\lambda^2 \tan\alpha}\left(\frac{1}{N} - \frac{1}{N^2}\right) + \frac{2p}{3\pi\lambda} - \frac{p^{3/2}}{8\sqrt{\pi N}\lambda^{3/2}}$$
$$+ \pi\ln\left(\frac{p}{4r_c}\right) + 2C_1, \tag{33}$$

$$\frac{E_p}{K} = \frac{p^2}{12\lambda^2 \tan\alpha}\left(\frac{1}{N} - \frac{1}{N^2}\right) + \frac{2p}{3\pi\lambda} - \frac{p^{3/2}}{4\sqrt{\pi N}\lambda^{3/2}} + C_2. \tag{34}$$

The leading contributions are produced by the B terms (31),(32), and the core energies (13),(14). Comparing these two, see also Fig. 6, one finds the critical number of cholesteric half layers N_c and the thickness h_c of the cell above which the lattice is composed of $b = p$ dislocations,

$$\alpha N_c \approx \frac{1}{16\left[\pi\ln\left(\frac{p}{4r_c}\right) + 2C_1 - C_2\right]}\left(\frac{p}{\lambda}\right)^2 \quad \text{or}$$

$$\frac{\alpha h_c}{p} \approx \frac{1}{32\left[\pi\ln\left(\frac{p}{4r_c}\right) + 2C_1 - C_2\right]}\left(\frac{p}{\lambda}\right)^2. \tag{35}$$

For the material under study, Frank constants of bend and twist are $K_3 = 15.4$ pN and $K_2 = 7.9$ pN, respectively, so that $\lambda/p = (1/2\pi)\sqrt{3K_3/8K_2} \approx 0.14$. Furthermore, experimentally, $k = \alpha h_c/p = 0.08$. Therefore, Eq. (35) predicts $\pi\ln(p/4r_c) + 2C_1 - C_2 \approx 21$. The latter estimate is in a good agreement with the energies expected by the model of the split dislocation core. Really, according to this model, Eq. (13) and Eq. (14), for typical $p \approx 5$ μm and $r_c \approx 5$ nm, and for the expected $C_1 \approx 0.4$ and $C_2 \sim 1$, one obtains $\pi\ln(p/4r_c) + 2C_1 - C_2 \approx 17$, close to the value 21 deduced from Eq. (35).

V. CONCLUSIONS

We visualized the 3D director patterns associated with defects in cholesteric Grandjean-Cano wedges with strong surface anchoring. The FCPM technique allows to establish the fine details of the dislocation structures. The dislocation of Burgers vector $b = p/2$ (the "thin line") splits into $\tau^{-1/2}\lambda^{+1/2}$ disclination pair; while $b = p$ (the "thick" line) splits into a $\lambda^{-1/2}\lambda^{+1/2}$ pair. In equilibrium, a lattice of $b = p/2$ dislocations is stable at $h < h_c$. At $h > h_c$ it is re-

placed by a lattice of $b = p$ dislocations. Metastable structures are also observed, such as apparent "thick" lines of total Burgers vector $b = p/2$ split into four disclinations $\lambda^{-1/2}\lambda^{+1/2}\tau^{+1/2}\lambda^{-1/2}$ and dislocations of zero Burgers vector, commonly composed of two $\lambda^{-1/2}$ and two $\lambda^{+1/2}$ disclinations. Kinks are different for $b = p/2$ and $b = p$ dislocations. In the $b = p/2$ case, the kink is only slightly tiled with respect to the dislocation; it is confined to the glide plane and is relatively long, $w \sim (5-10)$ p, as the core energy per unit length of $\tau^{-1/2}\lambda^{+1/2}$ pair is large as compared to the Peierls-Nabarro barrier associated with modifications of the $\tau^{-1/2}\lambda^{+1/2}$ core into a $\lambda^{-1/2}\tau^{+1/2}$ core. In the $b = p$ case, the kinks are short, $w \sim p$; both λ disclinations deviate from the glide plane, to preserve a nonsingular director structure. Thermal nucleation of kinks in cholesteric samples with p in the micron range is unlikely; kinks can be introduced by mechanical irregularities and during the filling of the sample. Kinks are responsible for glide of dislocations that never glide as straight lines. In contrast, climb occurs easily; dislocations in equilibrium are separated by well-defined distances along the bisector.

We employed the coarse-grained linear elastic model of cholesteric phase to calculate (a) the energy of layer distortions around the dislocations, which is valid for other cases, such as Sm-A; (b) corrections to the energy caused by finite thickness of the sample; (c) Peach-Koehler forces acting on a dislocation shifted from its equilibrium positions; (d) the Peierls-Nabarro friction associated with the split core of the cholesteric dislocations; (e) the critical thickness h_c. Comparison with the experimental data shows that the model of dislocation core split into a pair of disclination is adequate to describe the observed properties of defects.

Note finally that the features of dislocations described in this paper are specific for strong planar surface anchoring of the director at the bounding plates; under weak anchoring, the dislocation structures and behavior are completely different; in particular, dislocations are always of a nonsingular core and can be pushed away from the sample [47].

[1] P. G. de Gennes and J. Prost, *The Physics of Liquid Crystals* (Clarendon Press, Oxford, 1993).

[2] T. C. Lubensky, Phys. Rev. A **6**, 452 (1972).

[3] M. Kleman, *Points, Lines and Walls in Liquid Crystals, Magnetic Systems and Various Ordered Media* (Wiley, Chichester, 1983).

[4] M. Kleman, Rep. Prog. Phys. **52**, 555 (1989).

[5] O. D. Lavrentovich and M. Kleman, in *Chirality in Liquid Crystals*, edited by C. Bahr and H. Kitzerow (Springer-Verlag, New York, 2001).

[6] M. Kleman and O. D. Lavrentovich, *Soft Matter Physics: An Introduction* (Springer-Verlag, New York, 2002).
 [7] F. Grandjean, C.R. Hebd. Seances Acad. Sci. **172**, 71 (1921).
 [8] G. Friedel, Ann. Phys. **18**, 273 (1922).
 [9] R. Cano, Bull. Soc. Fr. Mineral. Cristallogr. **90**, 333 (1967).
[10] R. Cano, Bull. Soc. Fr. Mineral. Cristallogr. **91**, 20 (1968).
[11] P. G. de Gennes, C. R. Seances Acad. Sci., Ser. B **266**, 571 (1968).
[12] Orsay Liquid Crystal Group, Phys. Lett. **28A**, 687 (1969).
[13] M. Kleman and J. Friedel, J. Phys. Colloq. **30**, C4-43 (1969).
[14] T. J. Scheffer, Phys. Rev. A **5**, 1327 (1972).
[15] Y. Bouligand, J. Phys. (France) **35**, 959 (1974).
[16] G. Malet and J. C. Martin, J. Phys. **40**, 355 (1979).
[17] S. Masuda, T. Nose, and S. Sato, Liq. Cryst. **20**, 577 (1996).
[18] D. N. Stoenescu, H. T. Nguyen, P. Barois, L. Navailles, M. Nobili, Ph. Martinot-Lagarde, and I. Dozov, Mol. Cryst. Liq. Cryst. **358**, 275 (2001).
[19] R. Holyst and P. Oswald, Int. J. Mod. Phys. B **9**, 1515 (1995).
[20] G. Durand (private communication).
[21] P. Oswald and P. Pieranski, *Les Cristaux Liquides, Tome 1* (Gordon and Breach Science Publishers, Paris, 2000), p. 522.
[22] F. Nalet and J. Prost, Europhys. Lett. **4**, 307 (1987).
[23] Z. Li and O. D. Lavrentovich, Phys. Rev. Lett. **73**, 280 (1994).
[24] O. D. Lavrentovich and D.-K. Yang, Phys. Rev. E **57**, R6269 (1998).
[25] T. Ishikawa and O. D. Lavrentovich, Phys. Rev. E **63**, 030501(R) (2001).
[26] T. Ishikawa and O. D. Lavrentovich, in *Defects in Liquid Crystals: Computer Simulations, Theory and Experiments*, Vol. 43 of *NATO Advanced Study Institute, Series II: Mathematics, Physics, and Chemistry*, edited by O. D. Lavrentovich, P. Pasini, G. Zannoni, and S. Žumer (Kluwer Academic Publishers, Dordrecht, 2001).
[27] I. I. Smalyukh, S. V. Shiyanovskii, and O. D. Lavrentovich,

Chem. Phys. Lett. **336**, 88 (2001).
[28] S. V. Shiyanovskii, I. I. Smalyukh, and O. D. Lavrentovich, in *Defects in Liquid Crystals: Computer Simulations, Theory and Experiments*, Vol. 43 of *NATO Advanced Study Institute, Series II: Mathematics, Physics, and Chemistry* (Ref. [26]).
[29] I. Heynederickx, D. J. Broer, and Y. Tervoort-Engelen, Liq. Cryst. **15**, 745 (1993).
[30] Yu. A. Nastishin, R. D. Polak, S. V. Shiyanovskii, V. H. Bodnar, and O. D. Lavrentovich, J. Appl. Phys. **86**, 4199 (1999).
[31] F. Z. Yang, H. F. Cheng, H. J. Gao, and J. R. Sambles, J. Opt. Soc. Am. B **18**, 994 (2001).
[32] See, e.g., R. H. Webb, Rep. Prog. Phys. **59**, 427 (1996).
[33] I. Janossy, Phys. Rev. E **49**, 2957 (1994).
[34] W. E. Ford and P. V. Kamat, J. Phys. Chem. **91**, 6373 (1987).
[35] P. Yeh and C. Gu, *Optics of Liquid Crystal Displays* (Wiley, New York, 1999).
[36] B. A. Wood and E. L. Thomas, Nature (London) **324**, 655 (1986); S. D. Hudson and E. L. Thomas, Phys. Rev. A **44**, 8128 (1991).
[37] T. Ishikawa and O. D. Lavrentovich, Phys. Rev. E **60**, R5037 (1999).
[38] E. A. Brener and V. I. Marchenko, Phys. Rev. E **59**, R4752 (1999).
[39] P. G. de Gennes, C. R. Seances Acad. Sci., Ser. B **275**, 939 (1972).
[40] L. Lejcek and P. Oswald, J. Phys. II **1**, 931 (1991).
[41] M. S. Turner, M. Maaloum, D. Ausserre, J.-F. Joanny, and M. Kunz, J. Phys. II **4**, 689 (1994).
[42] R. Holyst and P. Oswald, J. Phys. II **5**, 1525 (1995).
[43] P. S. Pershan, J. Appl. Phys. **45**, 1590 (1974).
[44] J. Frieldel, *Dislocations* (Pergamon Press, New York, 1964).
[45] J. P. Hirth and J. Lothe, *Theory of Dislocations* (Wiley, New York, 1982).
[46] L. Lejcek, Czech. J. Phys., Sect. B **32**, 767 (1982).
[47] I. I. Smalyukh and O. D. Lavrentovich (unpublished).